

Principles of electron wave front modulation with two miniature electron mirrors

Krielaart, M. A.R.; Kruit, P.

DOI

[10.1016/j.ultramic.2021.113424](https://doi.org/10.1016/j.ultramic.2021.113424)

Publication date

2022

Document Version

Final published version

Published in

Ultramicroscopy

Citation (APA)

Krielaart, M. A. R., & Kruit, P. (2022). Principles of electron wave front modulation with two miniature electron mirrors. *Ultramicroscopy*, 233, Article 113424. <https://doi.org/10.1016/j.ultramic.2021.113424>

Important note

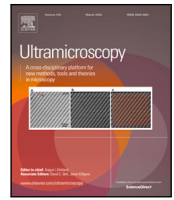
To cite this publication, please use the final published version (if applicable).
Please check the document version above.

Copyright

Other than for strictly personal use, it is not permitted to download, forward or distribute the text or part of it, without the consent of the author(s) and/or copyright holder(s), unless the work is under an open content license such as Creative Commons.

Takedown policy

Please contact us and provide details if you believe this document breaches copyrights.
We will remove access to the work immediately and investigate your claim.



Principles of electron wave front modulation with two miniature electron mirrors

M.A.R. Krielaart*, P. Kruit

Delft University of Technology, Faculty of Applied Sciences, Department of Imaging Physics, Lorentzweg 1, 2628 CJ Delft, The Netherlands

ARTICLE INFO

Keywords:

Electron wave front modulation
WKB approximation
Electron mirrors
Beam shaping

ABSTRACT

We have analyzed the possibilities of wave front shaping with miniature patterned electron mirrors through the WKB approximation. Based on this, we propose a microscopy scheme that uses two miniature electron mirrors on an auxiliary optical axis that is in parallel with the microscope axis. A design for this microscopy scheme is presented for which the two axes can be spatially separated by as little as 1 mm. We first provide a mathematical relationship between the electric potential and the accumulated phase modulation of the reflected electron wave front using the WKB approximation. Next, we derive the electric field in front of the mirror, as a function of a topographic or pixel wise excited mirror pattern. With this, we can relate the effect of a mirror pattern onto the near-field phase, or far field intensity distribution and use this to provide a first optical insight into the functioning of the patterned mirror. The equations can only be applied numerically, for which we provide a description of the relevant numerical methods. Finally, these methods are applied to find mirror patterns for controlled beam diffraction efficiency, beam mode conversion, and an arbitrary phase and amplitude distribution. The successful realization of the proposed methods would enable arbitrary shaping of the wave front without electron–matter interaction, and hence we coin the term virtual phase plate for this design. The design may also enable the experimental realization of a Mach–Zehnder interferometer for electrons, as well as interaction-free measurements of radiation sensitive specimen.

1. Introduction

The use of spatial light modulators [1] and digital micromirror devices [2,3] in light optics has enabled the controlled and dynamic shaping of photon beams. Methods for the shaping of charged particle beams are unfortunately not as versatile yet. To the electron microscopy community its development would provide many opportunities, such as beam mode conversion [4], or low-dose imaging of unstained biological specimen [5,6]. Recent experimental work indicates promising progress towards a programmable transmission-based phase plate [7] for use in transmission electron microscopy (TEM), although upscaling of the number of addressable pixels, as well as increasing the transmissivity of the phase plate, may prove challenging.

1.1. Electron wave front shaping

Electron wave front modulation is realized by passing the electron through an inhomogeneous optical medium, such as a spatially modulated electric field, or a topographically shaped phase plate. Electron beam shaping requires a medium that acts spatially on the phase of the electron wave front. The build-up of electrical charge at the surface

of this medium will influence the resulting wave front modulation, which is avoided by making use of electrically conducting materials only. Spatial coherence of the electron across the phase modulator can be realized by a combination of a high brightness source and a small beam current [8]. These requirements can be fulfilled in a number of ways.

Most commonly, electric and magnetic fields are used for charged particle beam deflection and focusing, which can be described as electron wave front manipulations. The fields are then generated external to the optical axis of the microscope and the use of electrically conductive elements prevents charging of the electrodes. Series of magnetic and electric multipole elements are seen in transmission electron microscopes and have been demonstrated to correct imaging system aberrations [9]. The combination of a multipole electrode with an annular aperture for vortex beam creation is reported as well [10].

Alternatively, patterned thin film amorphous carbon or silicon nitride membranes that cross the beam path can modulate the phase of the beam [11]. On the one hand this enables contrast enhancement [12], such as Zernike phase contrast [13,14], while on the other

* Corresponding author.

E-mail addresses: m.a.r.krielaart@tudelft.nl, mauricek@mit.edu (M.A.R. Krielaart).

hand beam mode conversion of plane waves into vortex beams [15–18], non-diffracting Bessel beams [19], and probability preserving Airy beams [20] are realized. Although transmission phase plates offer an increased flexibility for beam shaping with respect to externally generated fields, the limited operational life time and sensitivity to contamination [12,21] are still factors that limit the long-time application of these methods.

In contrast to the former methods that rely on transmission of the electron, electron mirrors slow down and reflect the incident beam prior to reaching the mirror electrode. This facilitates an alternative method to electron beam shaping that avoids electron beam–matter interaction. In the past, the use of tetrode electron mirrors for aberration correction [22] has been experimentally demonstrated [23]. Furthermore, mirror electron microscopy [24] has been successfully employed to measure the roughness of supersmooth surfaces, by electrically biasing the specimen just below the cathode potential of the source [25]. Also, it is suggested that a pixelwise deformable electron mirror could be used for adaptive phase contrast enhancement [26], and can as well be applied for electron beam lithography [27]. Electron mirrors are usually combined with a beam separator [28] in order to separate the trajectory of the incident and reflected electrons.

The drawbacks of transmission optics, such as phase plate contamination, operational life-time, electrical charge built up at surfaces and reduced optical transmissivity do not present themselves to mirrors. In comparison to transmission based techniques, the use of reflection based optics becomes increasingly advantageous when more than one reflective element is present in the beam line. The use of multiple beam reflective elements is seen with the recent development of an aberration corrected low energy electron microscope/photo-emission electron microscope (LEEM/PEEM) [29,30] instrument. Here, the mirror assemblies are mounted onto the microscope column under a 90 degree angle, which is a necessity due to the large volume claim of conventional beam separators.

More recent instrumentation developments allow for miniaturization of beam separators [31]. This enables for instance the realization of a proposal for aberration correction in scanning electron microscopy (SEM) based on two miniature electron mirrors [32]. The latter paper describes a miniature column with two parallel optical axes. The use of parallel optical axes enables one to reduce the deflection angles in the beam separator to below 100 mrad. In turn, this limits the deflection dispersion in the corrector, that may ordinarily limit the performance of such instrument [28].

The miniature mirrors in the above mentioned proposal for aberration correction may be replaced by mirrors that contain freely chosen patterns. For the resulting optical setup, we coin the term *virtual phase plate*. In this work, we describe the influence that the mirror pattern topography has on the phase modulation of the reflected electron, and then turn it around to find the surface topography or voltage distribution for a required wave front shape. The results are demonstrated by means of numerical examples.

2. Phase modulation with an electron mirror

Electrons are decelerated by an electrode with a negative electric potential that spans across the propagation axis. At a sufficiently negative electrode potential, the incident electron is completely stopped and will be reflected back towards the direction of origin. This requires an equipotential value that equals that of the extraction voltage at the electron source. As the electric field in front of the mirror electrode must satisfy the Laplace equation, the velocity of the electron gradually changes as it approaches the mirror electrode. Hence electron mirrors are characterized by ‘soft’ reflection fields that act as inhomogeneous refractive medium [33]. This is different from mirrors in light optics, for which a ‘hard’ reflection of the photon at the mirror surface takes place.

The electric field in front of the mirror electrode satisfies the Laplace equation, and thus any spatial topographic or charge pattern at the mirror electrode will result in the spatial modulation of the electric field in front of the electrode as well. As the electric field of the mirror extends from the mirror electrode into the path of the incident electron beam, a continuous modulation of the wave front takes place as the wave front approaches the mirror. Non-flat, structured electron mirrors have the property to locally alter the phase of the wave front of a spatially spread out incident electron, and the quantum mechanical effect of a mirror perturbation [34], and periodic structures [35,36] have been studied in the past analytically and numerically. It was suggested that the use of controlled wave front modulation with arbitrarily patternable mirrors could be used for structural hypothesis testing [26], but this has to our knowledge not been demonstrated experimentally yet.

Here we will focus our attention to generalized mirror patterns and their resulting effect on the wave front of the reflected electron wave front. For this, we will first provide a relationship between the electric potential and the accumulated phase modulation of the reflected electron wave front. Next, we will derive the electric field in front of the mirror, as a function of the topographic or pixel wise excited mirror pattern. With this, we can then relate the effect of a mirror pattern onto the near-field phase, or far field intensity distribution and use this to provide a first optical insight into the functioning of the patterned mirror. We will conclude this section with a discussion on chromatic effects.

2.1. Electron phase as a function of electric potential

In transmission electron microscopy, the acceleration of the electron beam by the (mean inner) potential of a phase plate is usually small in comparison to the nominal beam energy. This justifies the use of the projection assumption, which describes the exit wave ψ_{out} after passing a plane wave electron through a phase plate as [37]

$$\psi_{out} = \exp(i\sigma V_z). \quad (1)$$

The term inside the exponent in [Eq. (1)] may be considered as a phase transfer function, as it describes in the essence the effect that the electric potential has on the phase of the transmitted electron. In this equation, σ is an interaction constant that is proportional to the electron wave length, and $V_z = V_z(x, y)$ is the projected potential along the propagation axis,

$$V_z(x, y) = \int_{-\infty}^{\infty} V(x, y, z) dz. \quad (2)$$

This approach does not work for electron mirrors, for a number of reasons. Foremost, the projection assumption is invalid as the mirror potential equals that of the beam energy. In addition, we note that the upper boundary of the integral is ill-defined, as the wave function of the electron will actually penetrate the mirror field to some extent behind the classical turning point. The situation complicates even further when the mirror electrode is not flat, but instead contains a spatial pattern.

2.1.1. Convolution model

Earlier work related to mirror electron interference microscopy has resulted in a relationship between the mirror profile $h(x, y)$ and the phase modulation $\phi(x, y)$ of the reflected beam [25,38]. It was demonstrated that under the assumption $h \ll z_R \ll z_1$, with the mirror electrode at $z = 0$ and the field limiting aperture electrode at z_1 , and with z_R the coordinate plane of reflection, or turning point, in front of the mirror surface, that the phase difference between the reflected object and reference beam in a mirror electron interference microscope can be obtained through [35],

$$\phi(x, y) = \frac{2\pi}{\lambda_e} \times [h(x, y) * G(x, y, z_R)]. \quad (3)$$

In the equation, $G(x, y, z_R)$ is called the blurring function, and λ_e is the field free electron wave length. The blurring function as a function

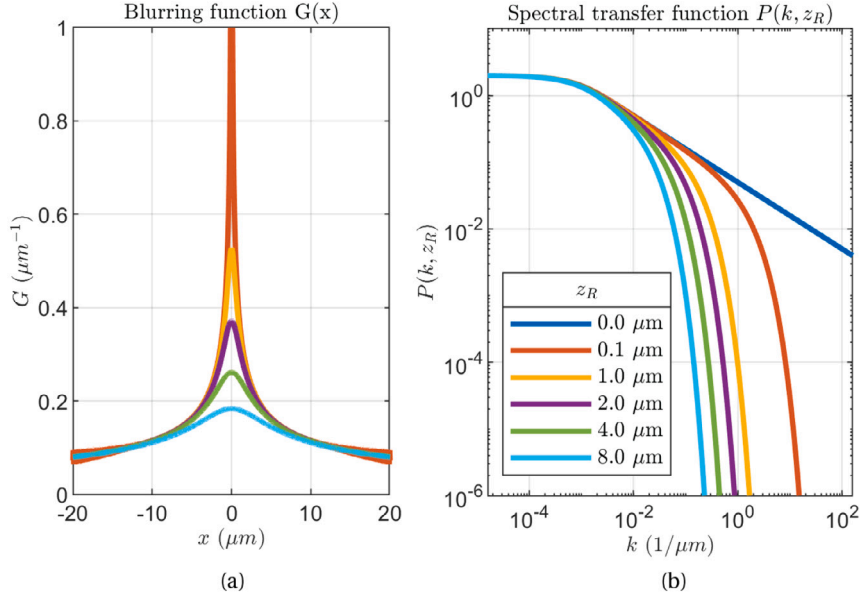


Fig. 1. (a) Blurring function $G(x, z_R)$, and (b) Spectral transfer function $P(k, z_R)$, for different values of turning point coordinates z_R . Plot and calculations based on methods described in [38] that we reproduced here from [25].

of one transverse spatial dimension is plotted in [Fig. 1(a)] for a range of turning point coordinates. From the plot it is observed that the blurring function becomes steeper when the turning point of the beam is positioned closer to the mirror substrate. The increased steepness of the curve renders the convolution more sensitive to high spatial frequency components residing in the mirror pattern, as the beam is reflected closer to the mirror electrode.

The blurring function is the Fourier transform of the ‘spectral transfer function’ $P(k, z_R)$, which is given by [25]

$$P(k, z_R) = \sqrt{\frac{\pi}{kz_1}} \times \exp(-kz_R) \times \text{erf}\left(\sqrt{kz_R}\right). \quad (4)$$

This function provides a direct relation between the attenuation of different spatial components at a fixed mirror bias potential. The spectral transfer function is plotted in [Fig. 1(b)], for a linear electric field strength of 10 kV/mm that we assume throughout our work.

2.1.2. WKB approximation

The derivation of the convolution method is based on the analytical work in [38]. There, the WKB approximation is used under the assumption of transverse mirror pattern components that do not exceed the distance of closest approach of the electron towards the mirror electrode. Consequently, the validity of the original convolution model is limited to $h \ll z_R \ll z_1$, and thus potentially reduced when micromachined electron mirrors are considered for which $h \lesssim z_R$. Instead, we here apply the WKB method numerically, such that we are not limited by linearizations needed in the analytical work of [38], and in that way study the extent of the validity of the convolution model beyond the restriction $h \ll z_R \ll z_1$.

The WKB approximation assumes the separability of the amplitude $a(\vec{r})$ and phase $\phi(\vec{r})$ of the wave function in the form $\psi(\vec{r}) = a \exp(i\phi)$, for which it is then demonstrated that the phase distribution is related to the scalar electric field through [39],

$$\phi(x, y) = \hbar^{-1} \int_{z_1}^{z_R(x, y)} p(x, y, z) dz = \hbar^{-1} \int_{z_1}^{z_R} \sqrt{2m_e(\mathcal{E} - V(x, y, z))}. \quad (5)$$

The classical momentum $p(x, y, z)$ of the electron with field-free energy \mathcal{E} is integrated along paths that run in parallel with the optical axis. For an incident plane wave, the electron trajectory is defined to coincide with the z -axis here. The classical momentum is related to the scalar electric field (U) through the potential energy function,

$V = eU(x, y, z)$. The integration is performed between the coordinates of the field limiting aperture z_1 and the classical turning point $z_R(x, y)$. The classical turning point coincides with the lateral coordinate, at which the electric potential equals that of the extraction voltage of the electron source ($\mathcal{E} = V$), and this is influenced by the electric perturbations due to the pattern at the mirror electrode.

In order to assess the effect that the pattern at the mirror electrode has on the phase of the reflected electron, we suggest to treat the contributions from the mirror pattern in terms of its Fourier components. This approach is similar to what we have used in previous work, where we demonstrated the agreement between the obtained magnitude of phase modulation through the WKB method and direct solutions to the Schrödinger equation [36], and note that solutions through the WKB method are less computationally expensive. Then the spatial phase modulation may be obtained for every component of the field separately. For a modulus of spatial frequency $k = |\vec{k}|$ at the pattern, this surmounts to finding the integrated phase difference A_k of the two electron trajectories that coincide with the crest and trough of the component of the field, given as

$$A_k = \phi(0) - \phi(1/(2k)). \quad (6)$$

In this expression, A_k denotes the amplitude of the phase modulation associated with spatial frequency k , and essentially corresponds to the maximum of phase difference that would result from application of the convolution model in [Eq. (3)]. The integration boundary z_R in [Eq. (5)] is different for both terms in [Eq. (6)] as the electron approaches the mirror electrode closer at the trough of the modulated electric field. The values of z_R corresponding to the trough and crest of the field can be obtained analytically through the Lambert-W function [see Appendix A], or numerically by solving for $U(z) = E$. The complex wave function after reflection associated with this solution is reconstructed by,

$$\psi(k) = \exp(iA_k \cos(2\pi kr + \theta_k)). \quad (7)$$

This expression may be compared to Eq. (31) in [35], where the effect of a single harmonic perturbation at a mirror surface was studied. The full wave function of the incident initial plane wave when exiting the reflection field is then described by the sum of all harmonic components that are present in the pattern at the mirror electrode, and

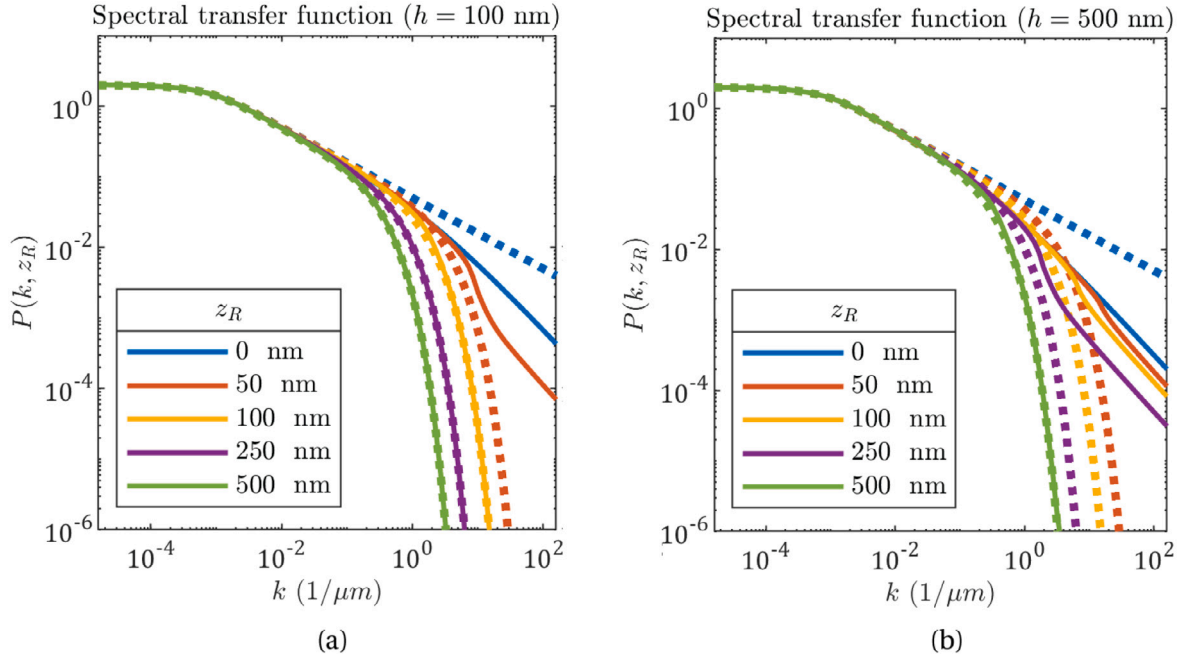


Fig. 2. Spectral transfer function obtained through the convolution model (dashed lines) and WKB approximation (solid lines), at a profile height of (a) 100 nm, and (b) 500 nm, as a function of spatial frequency k and closest approach z_R .

generalizes to

$$\psi_M(r) = \exp\left(i \sum_{n=0}^{\infty} A_{k_n} \cos(2\pi k_n r + \theta_{k_n})\right). \quad (8)$$

The angle θ_k fixes the relative position of each term with respect to other spatial contributions in the pattern.

2.1.3. Validity of the convolution model

We can now directly compare the phase modulation that is obtained through the convolution model to that of the WKB approximation. This comparison may offer a more quantitative bound on the restriction $h \ll z_R \ll z_1$ that is placed on the validity of the convolution based model. For this, we obtain the phase modulation through the WKB method for a number of pattern heights, and normalize the obtained data to the lowest spatial frequency that we analyze. Note that the spectral transfer function [Eq. (4)] in the convolution model is not dependent on the pattern height, and can thus be obtained at once.

In [Fig. 2] we have plotted the spectral transfer function that is obtained from the convolution model (dashed lines) and the WKB approximation (solid lines), at a linear electric field strength of 10 kV/mm. In the comparison, we assumed $z_1 = 200 \mu\text{m}$ and a pattern height of (a) 100 nm, and (b) 500 nm. The distance of closest approach towards the mirror electrode (z_R) is varied between 0 and 500 nm in this analysis.

In both data sets we observe that the two models are in good agreement in general. However, when $z_R \leq 2h$ we start to observe a deviation. It is thus in principle possible to use the convolution model, as long as the former strict inequality is satisfied. We choose to use the WKB method instead in the remainder of this work.

2.1.4. Far field intensity at one spatial frequency

In the following we relate the near field phase modulation to the resulting intensity in the far field. The far field intensity can be obtained through Fresnel propagation of ψ_M . We can also place a lens in front of the mirror, and use a Fourier transform to obtain the intensity distribution at the image plane that coincides with the focal plane of this lens. The resulting far field diffraction intensity of a WKB phase modulation amplitude A_k can be obtained directly through the Jacobi–Anger relationship, that expands a modulated complex exponential on

the left hand side into an infinite sum that contains Bessel functions $J_n(\xi)$ of order n on the right hand side [40],

$$\exp(i\xi \cos(\chi)) = \sum_{n=-\infty}^{\infty} i^n J_n(\xi) \exp(in\chi). \quad (9)$$

The infinite sum may be interpreted as a Fourier series, which results in that the intensity of diffraction spots at the far field due to the single spatial frequency k is given explicitly by $|J_n(A_k)|^2$ where n labels for the harmonic tones of k . In [Fig. 3(a)] we show the intensity of the unscattered ($n = 0$) and the first (green triangles), second (blue squares), and third (gray stars) order scattered beam intensities, as a function of phase modulation amplitude A_k . From this figure it is apparent that a single spatial frequency in the mirror pattern results in a set of diffraction spots, with intensities that cannot be chosen independently.

A practical limit of phase modulation amplitude emerges from the Jacobi–Anger expansion, above which it becomes no longer possible to modulate the intensity of a diffraction spot with only a single spatial frequency in the mirror pattern, without generating higher order spots as well. If we allow for 1% of the intensity to be directed into a higher order diffraction spot at the image plane, the amount of phase modulation that can be achieved with a single spatial frequency is upper bound to $\pi/6 \approx 0.5$ rad [Fig. 3(b)]. Higher values of phase modulation are then only attainable, when the development of the higher harmonics is suppressed by adding to the fundamental pattern a $\theta = \pi$ rad out of phase contribution of the respective higher harmonic spatial frequencies.

2.1.5. Addition of multiple spatial frequencies

In the following we analyze the extent of the validity of using the results from [Eq. (9)] and [Fig. 3(a)] when multiple spatial frequency components are present in the mirror pattern. The result as shown in [Fig. 3(a)] is invariant for a change in spatial frequency k . Hence, we consider for instance the effect of combining two spatial frequencies that are both characterized by a phase modulation amplitude A_k of say $A_k = \pi/3$. From the data shown in [Fig. 3(a)] we observe that the intensity of the unscattered beam is reduced from 1 to approximately 0.58, thus an intensity reduction of $1 - 0.58 = 0.42$. Meanwhile, the

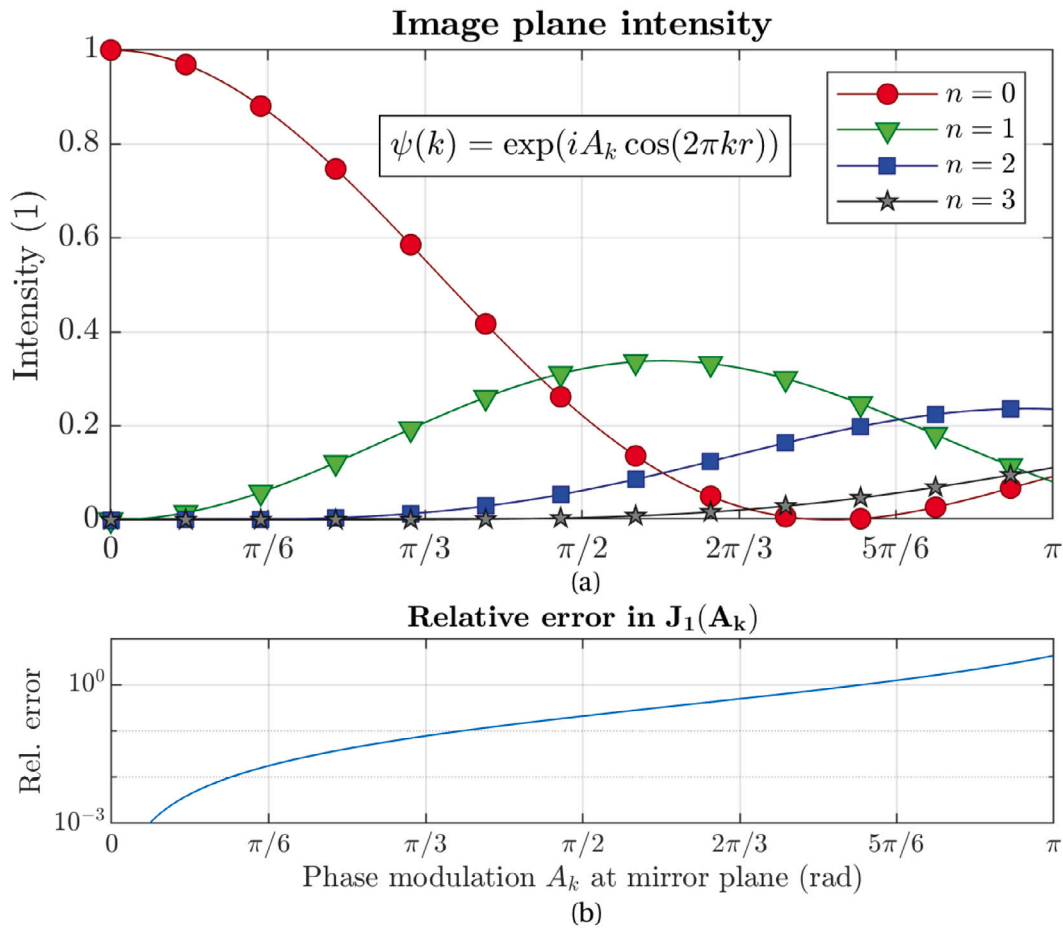


Fig. 3. (a) Intensity distribution at the image plane, as a function of phase modulation amplitude (A_k) for a single and fundamental spatial frequency k . Plotted orders n correspond to harmonic frequencies nk , with $n = 0$ representing the unscattered component of the beam. (b) Relative error of the intensity of the diffraction intensity due to the generation of higher order spots.

intensity in the first order diffraction spots related to both pattern components increases to approximately 0.20, yielding an apparent total intensity increase in the scattered beam of $2 \times 2 \times 0.20 = 0.80$. This suggests that intensity is created in the scattered beam, as a result of adding an additional pattern component. Where did this intensity come from?

It appears that linear addition of the effect of multiple pattern components yields physically incompatible results. We can understand this, by carefully analyzing the effect of multiple spatial frequencies when inserted into [Eq. (8)], and expanding into the far field intensities using [Eq. (9)]. For two given spatial frequency k_1 and k_2 (and $k_1 \neq k_2$) the near field wave front is described as

$$\begin{aligned} \psi_M(r) &= \exp(iA_k[\cos(2\pi k_1 x) + \cos(2\pi k_2 x)]) \\ &= \exp(iA_k \cos(2\pi k_1 x)) \times \exp(iA_k \cos(2\pi k_2 x)). \end{aligned} \quad (10)$$

In the far field, the intensities are then described by the product of the Jacobi–Anger expansion of both terms, given as

$$\begin{aligned} I &= \left\{ \sum_{n=-\infty}^{\infty} i^n J_n(A_k) \exp(in2\pi k_1) \right\} \times \left\{ \sum_{n=-\infty}^{\infty} i^n J_n(A_k) \exp(in2\pi k_2) \right\} \\ &= \left\{ \sum_{n=-\infty}^{\infty} c_{n,1} \exp(in2\pi k_1) \right\} \times \left\{ \sum_{n=-\infty}^{\infty} c_{n,2} \exp(in2\pi k_2) \right\}. \end{aligned} \quad (11)$$

Effectively, the result in [Eq. (11)] describes a product of two Fourier sums, which can generally be expressed as a convolution of its coefficients $c_{n,1}$ and $c_{n,2}$. From this it is concluded that the linear addition of the effect of multiple spatial frequency components in the pattern is not allowed in general. However, if only values of $A_k \ll 1$

are considered, the effect of the cross terms in the product in [Eq. (11)] become negligible, since then $J_0(A_k) \approx 1$. This can be made more explicit by considering two pattern components, that satisfy $k_2 = 2k_1$ and contribute a phase modulation amplitude A_{k_1} and A_{k_2} to the reflected electron. Then, the product in [Eq. (11)] can be evaluated explicitly for the lower order terms and yields the following intensities,

$$\begin{aligned} I_{\text{far field}} &\propto \begin{cases} [J_0(A_{k_1})J_0(A_{k_2})]^2 \sim 1 & \text{Unscattered beam} \\ [J_1(A_{k_1})J_0(A_{k_2})]^2 \sim J_1^2(A_{k_1}) & \text{First order of } k_1 \\ [J_0(A_{k_1})J_1(A_{k_2}) - J_2(A_{k_1})J_0(A_{k_2})]^2 \sim J_1^2(A_{k_2}) & \text{First order of } k_2. \end{cases} \end{aligned} \quad (12)$$

In this result, the similarity conditions are satisfied if and only if $J_0(A_{k_2}) \approx 1$ and $J_1(A_{k_1}) \approx 0$, thus in general when $A_{k_n} \ll 1$. We use this result as a justification for linear addition of the effect that multiple pattern contributions have on the phase of the reflected electron, and we believe that this result is in line with the weak phase object approximation [41] that is conventionally adhered to in the context of thin phase plates.

2.2. Electric field as a function of mirror pattern

In the following, a description for the electric scalar potential is derived as a function of topographic and pixel wise patterning. This requires a solution for the Laplace equation of the scalar potential $U(x, y, z)$ in transverse coordinates x and y , and beam propagation

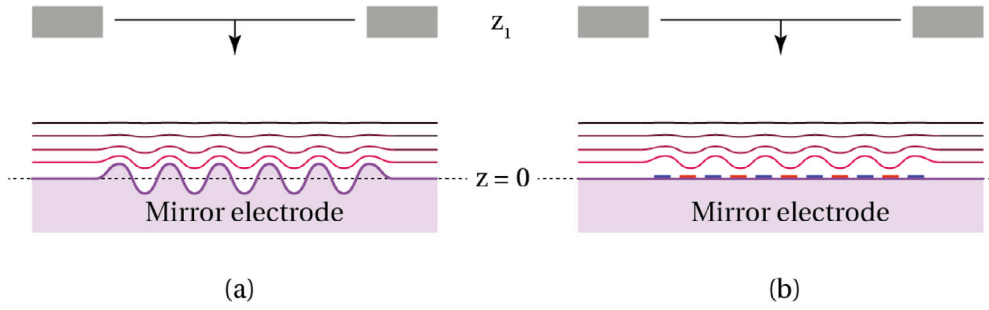


Fig. 4. Schematic geometry of the mirror electrode, in the case of (a) topographically patterned electron mirror and (b) pixel wise patterned electron mirror. The field limiting aperture at $z = z_1$ connects the mirror electric field to a region of constant potential u_1 .

direction z . It is assumed [also see Fig. 4] that the mirror electrode is positioned at $z = 0$ and the beam incidence and reflection takes place in the region for which $z < 0$. A field limiting aperture electrode is positioned at $z = z_1 < 0$, that connects the mirror electric field to a region of constant potential $U(x, y, z < z_1) = u_1$.

Solutions to the Laplace equation in Cartesian coordinates can be obtained through the method of separation of variables. The method ordinarily invites to look for solutions in the form $U(x, y, z) = X(x)Y(y)Z(z)$, but this will limit the shape of the pattern potential to products of $XY \simeq \cos(f(x)) \times \cos(g(y))$ that introduce a fixed grid of zero crossings. Instead, we will obtain solutions that describe the pattern with cross-terms, $U(x, y, z) = P(x, y)Z(z)$ in which $P(x, y)$ is the mirror pattern function, and $Z(z)$ describes the electric field attenuation above the mirror surface. We must then obtain a solution for

$$\frac{\partial^2 P(x, y)Z(z)}{\partial x^2} + \frac{\partial^2 P(x, y)Z(z)}{\partial y^2} + \frac{\partial^2 P(x, y)Z(z)}{\partial z^2} = 0. \quad (13)$$

This can be cast in the separated form given as,

$$\frac{1}{P(x, y)} \left[\frac{\partial^2 P(x, y)}{\partial x^2} + \frac{\partial^2 P(x, y)}{\partial y^2} \right] + \frac{1}{Z(z)} \frac{\partial^2 Z(z)}{\partial z^2} = 0 \Rightarrow C_p^2 + C_z^2 = 0. \quad (14)$$

The separation constants, $(C_p, C_z) \in \mathbb{C}$ must be allowed complex valued in order to satisfy the sum of separated squared coefficients. There are two boundary conditions that the above equation must satisfy:

1. At $z = z_0$ the potential distribution at the mirror electrode is described by $U_0(x, y, z) = u_0 + \Delta u_0(x, y, z_0)$ in the case of pixel wise patterning. Here, u_0 is the bias potential and $\Delta u_0(x, y)$ describes the (harmonic) potential variation across the mirror surface. In the case of topographic patterning, only a bias u_0 is present, and we approximate Δu_0 based on the pattern amplitude δ and the linear field strength $E_z = u_0/(z_1 - z_0)$, such that $\Delta u_0 = E_z \delta$. We choose $z_0 = 0$ is positioned at the origin of the coordinate system.
2. At $z = z_1 < 0$, a field limiting aperture electrode is positioned and it is assumed that at this point the scalar potential is uniform in the transverse direction, $U_1(x, y, z \leq z_1) = u_1$.

2.2.1. Solutions at the mirror electrode

The first boundary condition relates to the potential variation at the mirror electrode that is due to the pattern. A general solution for $P(x, y)$ is given (for constants p_0 and p_1) by

$$P_0(x, y) = p_0 \exp(i2\pi[k_x x + k_y y + \theta]) + p_1 \exp(-i2\pi[k_x x + k_y y + \theta]). \quad (15)$$

The coefficients k_x and k_y are spatial frequencies of the mirror pattern and θ is a constant phase offset. From [Eq. (14)], this provides the relationship

$$(2\pi i k_x)^2 + (2\pi i k_y)^2 = C_p^2. \quad (16)$$

From this it is seen that $C_p^2 < 0$ (since $k > 0$, and $i^2 = -1$) and consequently $C_z^2 > 0$. In the current form, [Eq. (15)] would allow

for only one spatial frequency in the mirror pattern. Solutions to the Laplace equation are linearly independent, which enables us to include multiple spatial components by linear addition,

$$P_0(x, y) = \sum_{(n,m)} F_{n,m} \cos(2\pi[k_{n,x}x + k_{m,y}y] + \theta_{n,m}). \quad (17)$$

Here we implicitly assume $p_0 = p_1 = 1/2$, such that the resulting sum of components represents a discrete Fourier sum of amplitudes $F_{n,m}$ and corresponding angles $\theta_{n,m}$. The amplitude term $F_{n,m}$ relates to the electric potential (in volt, Δu_0 in boundary condition 1) that the corresponding spatial frequency adds to the mirror potential, and its expression depends on the method of mirror excitation.

For topographic patterned mirrors, there is only the bias potential u_0 that is applied to the mirror electrode. The profile amplitude of the topographical features at the electrode surface ($\delta_{n,m}$) and the linear electric field strength $E_z = (u_1 - u_0)/(z_1 - z_0)$ is then used to approximate the effective potential at $z = z_0$. The local potential at $z = z_0 = 0$ is then approximated through the amplitude $\delta_{n,m}$ of the harmonic contribution and the linear field strength,

$$F_{n,m} = E_z \delta_{n,m}. \quad (18)$$

In the case of pixel wise applied potentials, the relationship between $F_{n,m}$ and the individual pixel potential is somewhat more complicated due to the finite size of the pixels. The set of potentials $\{u_p\}$ that is used to realize a harmonic variation across the entire mirror electrode then consists of discrete increments, rather than the smooth transition that is the case for topographic patterning. The high spectral frequency components that are associated with the harmonics of the individual pixels are neglected here, as we will demonstrate that such high spectral components (that is, smaller than the width of a single pixel) are not likely to significantly influence the phase of the reflected electron.

Next, a solution for $Z(z)$ must be obtained. Earlier we derived the requirement $C_z^2 > 0$ and this in turn yields the general solution,

$$Z_0(z) = \xi_1 \exp(2\pi k_z z) + \xi_2 \exp(-2\pi k_z z). \quad (19)$$

This leads to the relationship $C_z^2 = (2\pi)^2 k_z^2$ and we require $\xi_2 \rightarrow 0$ in order to prevent the potential from diverging in the region of reflection. In addition, the constant ξ_1 corresponds to the local potential value, $\xi_1 \equiv F_{n,m}$ for $z = z_0$. Finally, as $C_p^2 + C_z^2 = 0$, we obtain the common wave optical relationship $k_x^2 + k_y^2 = k_z^2$, from which we can construct the solutions for the Laplace equation that satisfy boundary condition 1) as,

$$U_0(x, y, z) = P_0(x, y)Z(z) = \sum_{(n,m)} \left\{ F_{n,m} \cos(2\pi[k_{n,x}x + k_{m,y}y] + \theta_{n,m}) \times \exp\left(-2\pi|z|\sqrt{k_{n,x}^2 + k_{m,y}^2}\right) \right\}. \quad (20)$$

2.2.2. Solutions at the field limiting aperture

A solution that satisfies the second boundary condition is less involved than that at the mirror electrode. It is assumed that the electric field is terminated at an equipotential surface that is flat in the plane perpendicular to the propagation (z) axis, such that the function $P_1(x, y) = \text{constant}$. In a practical situation, an aperture is needed at this plane that allows the electron beam to enter and exit the mirror field. The effect of this aperture is not treated here and may best be treated separately as part of a lens system in front of the mirror. The constant is absorbed into $Z_1(z)$, and we are thus only concerned with finding a solution for $Z_1(z)$, that has to satisfy

$$\frac{1}{Z_1(z)} \frac{d^2 Z_1(z)}{dz^2} = 0 \Rightarrow \frac{d^2 Z_1(z)}{dz^2} = 0. \quad (21)$$

The general solution is a first order polynomial, $Z_1(z) = az + b$. From the boundary conditions $Z(z_1) = u_1$ and $Z(z_0) = u_0$, a solution is readily obtained in the form of,

$$Z_1(z) = u_0 \left[1 - \frac{z}{z_1} \right] - \frac{u_1 z}{z_1}. \quad (22)$$

In this equation, the second term drops out under the assumption of a field-free region of constant potential at or beyond z_1 , for which $u_1 = 0$.

2.2.3. Analytical expression for the mirror electric scalar potential

A full solution for the electric potential that is created by a topographic or pixel wise patterned mirror is provided by addition of the separate solutions that were obtained, and is given in full as

$$\begin{aligned} U(x, y, z) &= P_0(x, y)Z(z) + Z_1(z) \\ &= \sum_{(n,m)>0} \left\{ F_{n,m} \cos(2\pi[k_{n,x}x + k_{m,y}y] + \theta_{n,m}) \right. \\ &\quad \times \exp\left(-2\pi|z| \sqrt{k_{n,x}^2 + k_{m,y}^2}\right) \left. \right\} \\ &\quad + u_0 \left[1 - \frac{z}{z_1} \right] - u_1 \frac{z}{z_1}. \end{aligned} \quad (23)$$

In this expression, we have shifted the contribution of the DC component of the mirror pattern outside of the sum, and it is now explicitly accounted for by the linear potential ramp provided by u_0 . The equation is applicable to both pixel wise and topographically patterned mirrors, and the elements in the sum only account for the spatial variations that resemble the surface topography.

The derived expression for the electric potential will be used in the calculation of the spatial phase modulation of a spread out beam that is reflected by this potential. The expression essentially describes a Fourier sum over all spatial frequencies that are contained in the mirror topography. The DC contribution outside the sum contains the linear potential ramp.

2.2.4. Qualitative influence of the pattern components on the phase modulation

We can now combine the obtained description of the mirror electric field [Eq. (23)] and the WKB approximation [Eq. (5)] and use this to obtain an initial qualitative understanding of the influence that the spatial frequency components of the mirror pattern have on the phase of the reflected electron. According to the WKB approximation the phase $\phi(\vec{r}) \propto \int \sqrt{U(\vec{r})} dz$. Because of the square root dependence, a direct solution that yields the phase modulation amplitude [as defined in Eq. (6)] as a function of the electric field modulation amplitude is not trivial. Instead, we will derive here an approximate analytical relationship between the mirror scalar potential and the resulting phase modulation and use this to obtain an initial understanding of the effect that the pattern frequency component has on the phase modulation amplitude. At a later stage a numerical implementation of [Eq. (6)] will be provided which serves as the basis of our pattern calculations.

Starting from the WKB approximation, we cast [Eq. (5)] into an alternative form:

$$\phi(x, y, z) = \hbar^{-1} \sqrt{2m_e e E} \int \sqrt{1 - U(x, y, z)/E} dz. \quad (24)$$

The square root inside the integral can be approximated by a power series for which the first terms are given below,

$$\sqrt{1-x} \approx 1 - \frac{1}{2}x - \frac{1}{8}x^2 - \frac{1}{16}x^3 - \mathcal{O}(x^4). \quad (25)$$

This approximation is valid and converges, provided that $|x| \leq 1$. Here, $x \equiv U/E$ satisfies the convergence condition, exactly up to the turning point of the beam where $U = E$ and thus the use of the approximation is justified.

The full evaluation of [Eq. (24)] requires to obtain the integral of the polynomial terms x^n , for which we use the electric scalar potential that from [Eq. (23)],

$$x^n = E^{-n} \left[F \cos(2\pi kr) \exp(-2\pi kz) + u_0 \left(1 - \frac{z}{z_1} \right) \right]^n. \quad (26)$$

As the integral over the terms in [Eq. (26)] is bounded by z_1 and z_R , it is noted that for terms $n > 1$ the exponential contribution quickly diminishes the cross terms, since

$$[\exp(-2\pi kz_R)]^n = \exp(-2\pi nkz_R) \rightarrow 0 \text{ for } 1/k \approx z_R, n > 1. \quad (27)$$

To understand at least qualitatively the effect that the single spatial frequency k has on the phase modulation, we can drop all but the first term in the expansion, even though this hinders us to quantitatively compare this initial result with any earlier work. The procedure yields the following result for the approximate integrated phase $\hat{\phi}$ along one axis,

$$\begin{aligned} \hat{\phi}(x_0, y_0, k) &= -\hbar^{-1} \sqrt{\frac{m_e e}{2E}} \int_{z_1}^{z_R} \left\{ F \cos(2\pi kr(x_0, y_0)) \exp(-2\pi kz) \right. \\ &\quad \left. + u_0 \left(1 - \frac{z}{z_1} \right) \right\} dz \\ &= -\hbar^{-1} \sqrt{\frac{m_e e}{2E}} \left[\frac{F \cos(2\pi kr(x_0, y_0)) \exp(-2\pi kz)}{-2\pi k} \right. \\ &\quad \left. + u_0 z \left(1 - \frac{z}{2z_1} \right) \right]_{z=z_1}^{z=z_R}. \end{aligned} \quad (28)$$

The net phase modulation amplitude for a single spatial frequency A_k [as defined in Eq. (6)], is obtained by evaluating the result in [Eq. (28)] at the crest and trough of the modulated electric potential, at which points $F \cos(2\pi kr) = \pm F$,

$$\begin{aligned} A_k &= \hat{\phi}(0, 0, k) - \hat{\phi}(1/(2k), 0, k) \\ &= -\hbar^{-1} \sqrt{\frac{m_e e}{2E}} \left(\frac{F}{2\pi k} [\exp(-2\pi kz_R^+) - \exp(-2\pi kz_R^-)] \right. \\ &\quad \left. + u_0 \left[z_R^+ - z_R^- - \frac{z_R^{2(+)} - z_R^{2(-)}}{2z_1} \right] \right). \end{aligned} \quad (29)$$

The contribution of the exponential terms at the lower boundary $z = z_1$ is set to zero explicitly here, since $1/k \ll z_1$, and z_R^\pm labels the turning point for the crest and trough of the field. An analytical form of the turning point coordinates is given in Appendix A, and can be obtained by solving $U(z) = E$ by means of the Lambert-W function [42].

From the obtained expression it is confirmed that, at equal excitation parameter F , higher spatial frequency components in the mirror electrode attenuate faster and consequently can modulate the reflected beam less than low spatial frequencies. This behavior could also be understood from the increased sharpening of the blurring function in [Fig. 1] as the electron reflects closer to the mirror electrode. Conversely, one may state that the turning point coordinate $z_R \rightarrow z_0$ must be positioned closer to the mirror pattern in order to have high spatial frequencies in the pattern influence the modulation of the phase of the reflected beam. The linear dependence $A_k \propto F$ demonstrates that

alternative to the former, the phase modulation in the reflected beam can also be increased by increasing the amplitude of the mirror profile, or the excitation potential in the case of pixelwise programmable mirrors.

2.3. Phase modulation as a function of pattern pitch and bias voltage

We have obtained a description of the scalar potential as a function of mirror topography [Eq. (29)], as well as a relationship between the scalar potential and the phase modulation [Eq. (5)] as a function of spatial frequency [Eq. (6)]. With that, we can now study the effect that the spatial frequency k , and the bias potential ΔU (with respect to the electron beam energy) has on the phase modulation amplitude of the reflected electron. For this, we are limiting ourselves to a maximum allowed electric field strength of 10 kV/mm, which is considered as a feasible value that should not result in electrical break down or arcing. In a setup that we are currently building [43], we aim at using a beam energy of 2 keV and hence the following results are also based on this value.

We have already found [Fig. 3] that the phase modulation amplitude must be kept small, and based on this we searched for a parameter space that fits this requirement. We consider that for a mirror pattern, spatial frequencies in the range of $k_0 \in [0.5 \dots 10] \mu\text{m}^{-1}$ can be manufactured for instance with ion beam lithography. In [Fig. 5] we show the phase modulation amplitudes that can be realized in this range of spatial frequencies, as a function of profile height amplitude and bias potential (in volt) with respect to the beam energy. This data has been obtained for a 2 keV electron beam energy and a linear field strength of 10 kV/mm. As a general trend, we observe an increase in phase modulation amplitude, as a function of both decreasing spatial frequency (increasing pattern pitch), as well as decreasing bias potential. An increase of the profile height amplitude is seen to lead to an increase of the phase modulation amplitude, and consequently to phase rollovers of 2π at increasing height values.

The obtained data indicates the sensitivity to phase modulation that may arise for instance due to non-flatness of the electrode wafer source material. This non-flatness may be introduced as a result of mechanical stress inside the material, and from the data shown in [Fig. 5] we see that this may especially pose a limitation for very low spatial frequency surface height modulation.

2.4. Mirror pattern as a function of target phase distribution

In a practical application of patterned electron mirrors, it is likely that the mirror pattern will be based on a desired or ‘target’ phase distribution $\phi_{\text{target}}(x, y)$ in the near field (diffraction plane). By obtaining the Fourier transform $\Phi_{\text{target}}(k)$ of this target distribution, the phase modulation amplitude $A_k = |\Phi_{\text{target}}(k)|$ of the target distribution is directly obtained in terms of the spatial frequencies that form the mirror pattern.

We make use of the proportionality $A_{k_0} \propto F \equiv \delta_k$, such that the reference pattern amplitude δ_0 [for instance, $\delta_0 = 1 \text{ nm}$ is shown in Fig. 5(b)] can be scaled directly to match the phase modulation amplitude A_k , by solving for δ_k in

$$\Phi_k = \frac{\delta_k}{\delta_0} \phi_{\text{WKB}}^{[\delta_0]} \quad (30)$$

In this equation, $\phi_{\text{WKB}}^{[\delta_0]}$ is the data set that contains the phase modulation amplitude as a function of bias voltage and spatial frequency of the mirror pattern, at a fixed reference profile amplitude δ_0 as shown before in [Fig. 5].

When the scaling is performed for each spatial frequency of the target phase distribution, the obtained pairs $\{\Phi_k, \delta_k\}$ return the complete description of the mirror pattern in Fourier space. The pattern is then

constructed in real space through a Fourier sum

$$P(x, y) = \sum_{(n,m)} \delta_{(n,m)} \cos(2\pi[k_{n,x}x + k_{m,y}y] + \angle\Phi_{k,(n,m)}). \quad (31)$$

The electric potential in front of the mirror substrate can be reconstructed in a similar approach.

2.5. Chromatic effects as a function of pattern parameters

Practical electron beams contain an inherent energy spread (about 0.6 eV for Schottky sources), and the value of this spread can be reduced by means of beam monochromatizing at the expense of beam current. The energy spread in the incident electron beam results in a deviation from the nominal turning point coordinate (z_R). As the modulation of the electric field decays exponentially as a function of this coordinate [Eq. (23)], the resulting phase modulation will deviate from the nominal target value.

We computed the effect of the beam energy spread through the WKB approximation. The calculation is performed on the basis of the data that was shown in [Fig. 5(b)] for a reference profile height of 1 nm. From this data, coordinate pairs of bias potential and spatial frequency $\{U_{\text{bias}}, k_0\}$ were collected that provide π phase shift at the nominal beam energy (the dashed black line in the plot). Next, the WKB approximation is performed numerically for the obtained parameter pairs, at varying beam energies in a range $E = E_0 \pm \Delta E_0$.

The obtained phase modulation as a function of the energy deviation ΔE_0 with respect to the nominal beam energy E and spatial frequency k that was obtained this way is shown in [Fig. 6]. This data indicates an increased sensitivity for phase dispersion towards higher spatial frequencies of the mirror pattern, and at increased energy deviation. Notably at spatial frequencies above $2 \mu\text{m}^{-1}$ a complete phase rollover of 2π already occurs within the 1 V analysis domain. This result suggests that it is necessary to monochromatize the beam. The required amount of energy filtering ultimately depends on the smallest feature size present in the pattern, as well as the application-dependent tolerance, as illustrated in [Fig. 6]. In addition, the data shown motivates the use of a high linear electric field strength as this leads to a reduced spacing between the equipotential surfaces that reflect the slower and faster parts of the beam. A linear field strength of 10 kV/mm that we used in the above analysis is generally considered as feasible in an electron optical setup.

3. Amplitude and phase modulation with electron mirrors

The electron mirror is the reflective counterpart of the transmission phase plate that is used in transmission electron microscopy. As the electron mirror fully reflects the incident wave front, the amplitude of the reflected wave front cannot be modulated at the mirror plane. A single electron mirror can thus be used for phase modulation only, and the effect of this phase modulation appears as an amplitude contrast at a diffraction plane of the mirror. This is good enough for many applications, however, in order to fully control the wave front, not only phase but also amplitude modulation must be realized.

Amplitude modulation in transmission optics is realized by using a comparatively thick amplitude mask that partially blocks the beam. This approach is not viable in the context of mirrors, as no absorption processes take place in front of the mirror. It is however possible to express the modulated phase of a wave front as amplitude contrast at a plane that is conjugated to that of the mirror, by means of defocusing the electron at this conjugate plane. The effect of a defocus of the beam at the conjugated plane is given by the phase contrast transfer function $\text{CTF} = \sin(\chi(u))$, in which [44],

$$\chi(u) = \frac{2\pi}{\lambda} \left(\frac{\Delta f \lambda^2 u^2}{2} + \frac{C_s \lambda^4 u^4}{4} \right). \quad (32)$$

Here, λ is the wave length of the electron, u the spatial frequency component of the modulated wave front, and Δf the amount of defocus.

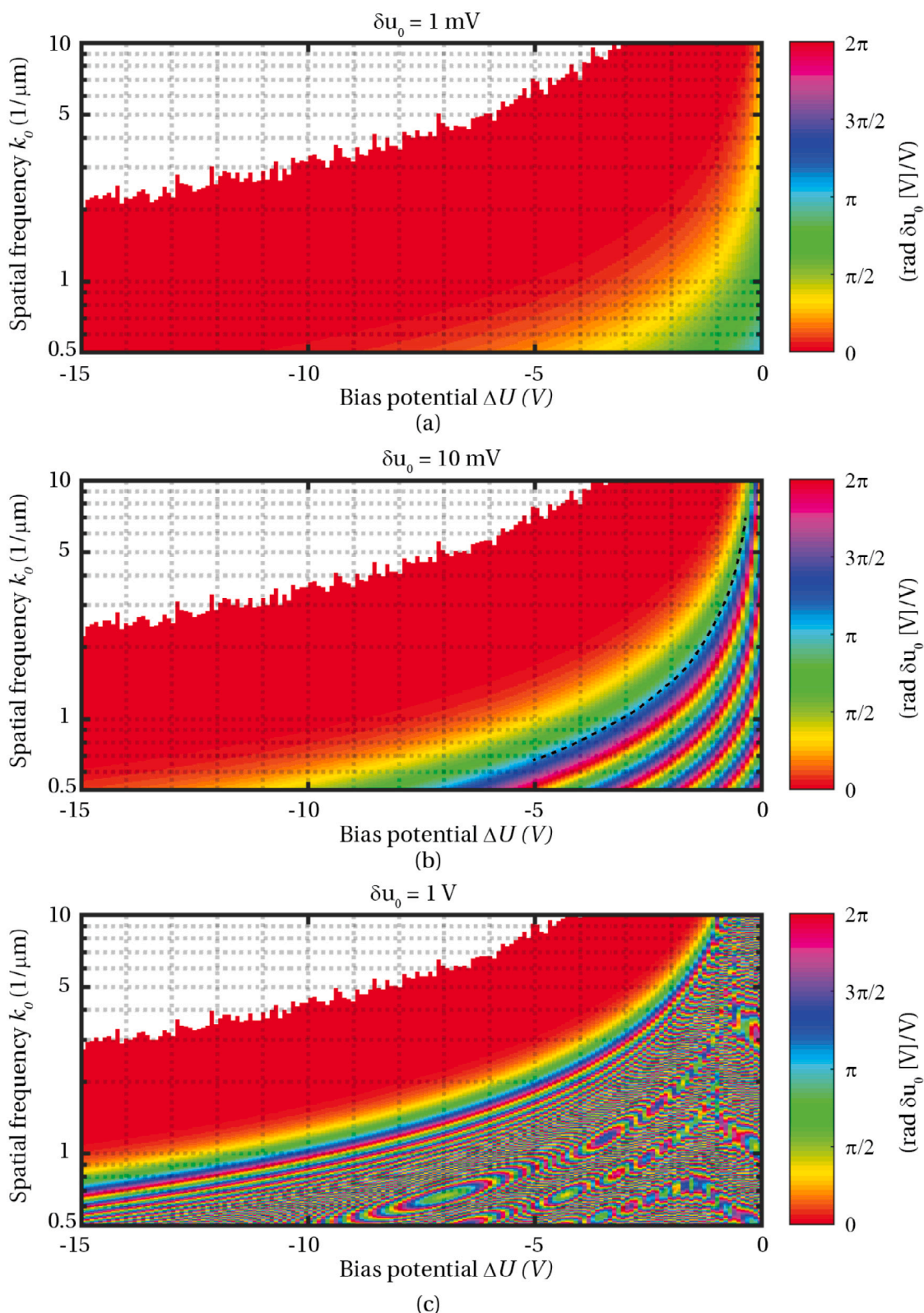


Fig. 5. Phase sensitivity of a reflected plane wave as a function of the bias potential (with respect to the beam energy) and spatial frequency component of the pattern, for a reference profile pixel voltage amplitude δu_0 of (a) 1 mV (corresponds to 1 Å height variation), (b) 10 mV (corresponds to 1 nm height variation), and (c) 1 V (corresponds to 100 nm height variation). A free electron energy of $E = 2 \text{ keV}$ and a linear field strength of 10 kV/mm is used in the calculation. The dashed black line in (b) indicates the line of constant phase that is used for the study of sensitivity to energy spread. Phase wrapping is performed on data that corresponds to a phase modulation greater than 2π .

The second term inside the brackets accounts for spherical aberration (C_s) of the imaging system in between the two conjugate planes.

When we position a second mirror at the plane conjugate to that of the first mirror, and in the absence of a defocus, i.e., $\Delta f = 0 \text{ mm}$, the wave front at a later image plane of the microscope is related to the

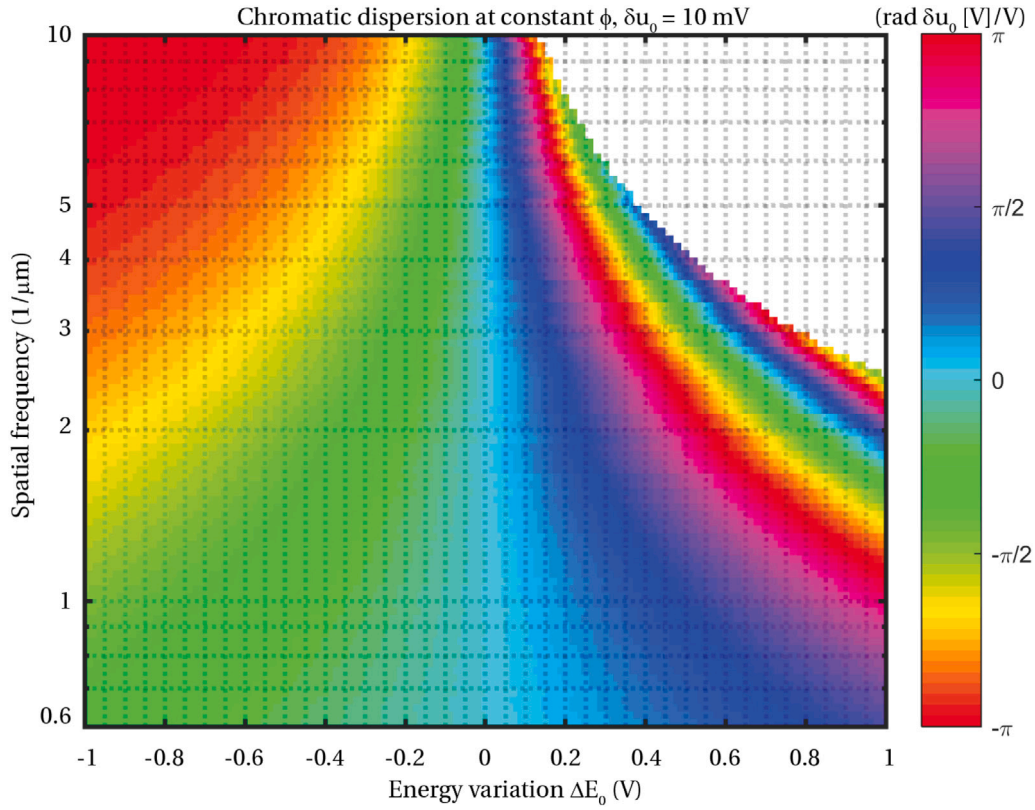


Fig. 6. Phase sensitivity of the reflected electron as a function of energy variation in the incident beam, for a range of spatial frequency components. Computations are performed for an equal target phase value of π rad, for data points that are indicated by the dashed black line in [Fig. 5(b)]. The color map labels the deviation of the phase as a function of energy variation ΔE_0 in the incident beam. Data obtained for a fixed profile amplitude of 1 nm, 2 keV nominal beam energy and linear field strength $E_z = 10$ kV/mm.

sum of the individual spatial phase contributions ϕ_{M1} and ϕ_{M2} due to mirror M1 and mirror M2,

$$\psi_{out} = \mathcal{F} \{ \psi_{in} \exp(i[\phi_{M1} + \phi_{M2}]) \}. \quad (33)$$

Here, $\mathcal{F}\{\cdot\}$ denotes a Fourier transform. From this expression it is apparent that only one mirror is in principle sufficient to perform phase only modulation, since the contributions of ϕ_{M1} and ϕ_{M2} to the output wave front are interchangeable and add linearly.

However, we reason that simultaneous amplitude and phase modulation is possible when two patterned mirrors are used. We will provide two alternative methods to achieve this. The first method relies on the CTF and the assumption that the two mirrors are placed at planes that are conjugate to each other. The second method assumes that the second mirror is placed at the diffraction plane of the first mirror.

We first consider the situation where the two mirrors are placed at optical conjugate planes, and the electron is spread out over the first mirror upon incidence. In this case, in the presence of a defocus of the reflected electron towards the second mirror, i.e., $\Delta f \neq 0$, the phase modulation due to the pattern at the first mirror expresses as an amplitude modulation as the electron is spread out over the surface of the second mirror. At the second mirror surface, local changes to the phase of the amplitude modulated beam can be realized by a proper choice of the pattern. However, we acknowledge that a genuine freedom of amplitude and phase is not attainable in this configuration, as the amplitude distribution is still limited by the CTF of the optical system.

Alternative to the above configuration, one may also consider to place the second mirror at the diffraction plane of the first mirror. The amplitude distribution in the diffraction plane is the Fourier transform of the phase pattern introduced by the first mirror. The second mirror now introduces the phase modulation to the beam.

3.1. Virtual phase plate based on two electron mirrors

A practical realization of the virtual phase plate requires the positioning of two electron mirrors and additional lenses inside the electron microscope column. An extensive discussion of integrating multiple electron mirrors in a microscope is provided recently by Dohi and Kruit [32]. From that work, it is concluded that through the use of miniature electron optical components it is possible to position the two mirrors at an axis parallel to the optical axis of the microscope. The coupling of the microscope and mirror axis trajectories can be performed by an electrostatic deflector, and two miniature Wien filter type deflectors. By making use of miniaturized optical components, the deflection angles can be kept small, such that deteriorating effects from deflection dispersions can be avoided.

In [Fig. 7] we show a schematic design for a virtual phase plate. In this schematic, the two mirrors are positioned opposite of each other on a common axis and the mirror patterns face each other. The mirror axis is parallel with the optical axis of the microscope. The coupling of the beam trajectory between the microscope axis and mirror axis can be performed with an electrostatic deflector that is positioned at the optical axis on the halfway plane in between the two mirrors, referenced to as the common cross-over plane (C.C.P.). The beam trajectory on the mirror axis demands a deflection towards and away from the mirrors that depends on the sign of the velocity vector (\vec{v}) of the beam. This sign dependent deflection could be realized by deflectors with crossed electric (\vec{E}) and magnetic (\vec{B}) fields if these fields are both perpendicular to each other and the beam path. When the electric and magnetic fields in such deflector satisfy the Wien condition ($\vec{E} = \vec{v} \times \vec{B}$), the resulting force on the electron beam enables either a straight passage or a deflection path for the beam, depending on the direction of incidence. The recent development of a miniature

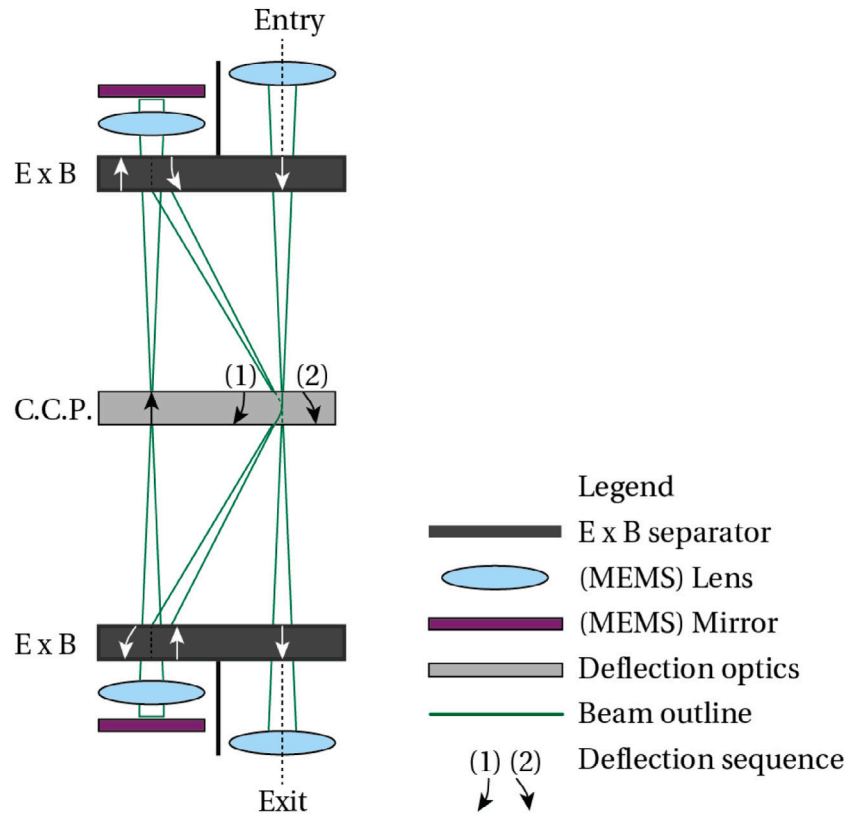


Fig. 7. Design of a double mirror system for integration inside (the column of) electron microscopes. The beam enters the setup on the microscope axis from the top. Coupling to the mirror axis is performed at the common crossover plane (C.C.P.) by means of an electrostatic deflector. Two Wien filter type beam separators ($E \times B$) are used to perform the direction-of-incidence dependent deflection at the mirror axis. After reflection at both mirror planes, the beam is coupled back to the optical axis and exits the setup on the microscope axis downwards, now with phase and amplitude modulation.

Source: Schematic reproduced from [31].

electron beam separator with two parallel axes can explicitly allow for the close proximity of both axes in the described scheme [31].

Remarkably, when the Wien condition for straight passage is also enforced onto the straight passages on the optical axis near the entry and exit, a full trip of a beam through the double mirror system does not suffer from deflection dispersion in first order at the common crossover plane. The system can be miniaturized by making use of MEMS technology, such that the deflection angles can be kept small (below 50 mrad) and thus suppressing deflection dispersions [32]. An in-depth electron optical and mechanical description of the system is provided in [43].

4. Application examples for electron mirrors

We demonstrate possible applications for patterned electron mirrors. Throughout this section we assume a beam energy of 2 keV and a linear electric field strength of 10 kV/mm in the mirror region. These numbers are based on a proof of principle experiment that we are currently designing. Details about the numerical methods that were used to obtain the results in the following sections are presented in Appendix B.

4.1. Zernike phase mirror

The use of a Zernike phase plate in TEM results in a change to the contrast transfer function provided in [Eq. (32)] as given by [44],

$$\text{CTF} = \sin(\chi(u)) \rightarrow -\cos(\chi(u)) \text{ for } u > u_h. \quad (34)$$

In words, the equation states that the contrast is enhanced from near-zero to near unity for spatial frequencies u that exceed the modulus of the spatial frequency u_h of the central hole in the phase plate.

The mirror equivalent of such Zernike phase plate would require an alteration in the reflected beam such that the unscattered (on-axis) component is shifted $-\pi/2$ rad with respect to the scattered wave components.

In the past it is already suggested that this could be achieved with a pixel wise programmable mirror simply by applying a bias in the order of 70 mV (assuming a linear field strength of 10 kV/mm) to the central pixel [26], and here we apply the method that we derived above to the same model system. As we only aim to shift the phase of the unscattered beam, the desired phase profile shows resemblance with a top hat function and it should thus be expected that a large number of spatial frequencies is involved in the resulting mirror topography.

The result of the analysis is shown in [Fig. 8] for an assumed 200 nm hole size in the Zernike phase plate. We observe a peak in excitation close to the optical axis that is representative of this hole size, followed by a damped oscillation of higher harmonic contributions. It should be noted that the effective value for u_h is determined in the case of an electron mirror by the focal distance of the mirror-lens system towards the image plane. For instance, one could increase the spread out the wave front over the mirror surface, thereby effectively increasing the magnification. If the mirror topography is not scaled laterally by an equal factor, this effectively changes the range of spatial frequencies in the reflected wave front that are phase shifted by the Zernike mirror pattern.

4.2. Tuning diffraction efficiency

The origin of this work stems from the question if interaction-free measurements [45] can be performed with electrons [46] in a practical manner, in order to reduce electron beam induced radiation

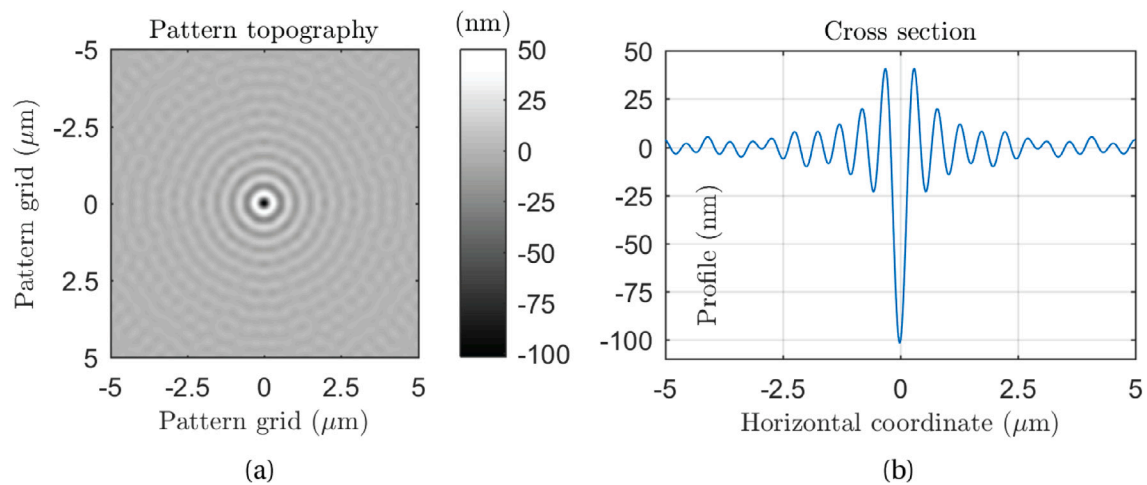


Fig. 8. Mirror topography for Zernike phase manipulation. (a) Full field reconstruction of the pattern, for a bias potential of 7 V with respect to the beam energy. (b) Cross section of the reconstructed pattern, through the center of the topography.

damage [47] in electron microscopy [48]. Subsequent proposals for designs of a quantum electron microscopes [49,50] that could perform this type of experiment introduces the need for a two-port diffractive element for electron beams [51]. The electron grating mirror is one means to this end, but in its current form suffers from the disadvantage of generating a two-sided diffracted beam, instead of the targeted one-sided first order diffracted beam [36].

Here we study how the diffraction efficiency of the intensity that is directed into the first order spot can be maximized, while at the same time keeping the intensity in the higher order spots to a minimum. We already discussed the effect of a single spatial frequency at the mirror pattern that would result from a sinusoidal pattern, and concluded that the intensity of the resulting diffraction spots are provided by the squared Bessel function of the respective diffraction order as a function of phase modulation amplitude (A_k) [ref. Eq. (9)], and dashed line in Fig. 9].

The generation of the higher order diffraction spots could be in principle suppressed, by adding higher order spatial frequency components to the mirror pattern. These pattern components must cancel the out-of-phase contribution to their respective diffraction spot at the image plane, with respect to the higher harmonic spot that is due to the fundamental pattern frequency.

Numerically the pattern that is required for this is found by providing a target image plane distribution consisting of only a central spot and the two first order diffraction spots. The target phase of the central spot relative to the two first order diffraction spots is set to $-\pi/2$, which is a physical requirement for a first order diffracted beam when only a single mirror reflection takes place [also see Sections 3 and 2.1.4]. The image plane distribution is then Fresnel propagated to the diffraction plane, in order to obtain the amplitude and phase modulation that must be provided for by the mirror pattern.

We have performed this computation using two different approaches. First, we considered the use of only one mirror, thus limiting ourselves to phase-only modulation. The obtained diffraction spot intensities that could be realized this way are plotted in [Fig. 9] with circle markers. The range of phase modulation amplitude values that are shown in the plot are realized by adjusting the ratio of the targeted central and diffracted spot amplitudes at the image plane. The target image plane distribution is propagated towards the mirror plane, at which we obtain the plotted phase modulation amplitude as the largest absolute phase difference at this plane. Note that this definition for $A_{\{k\}}$ is somewhat broader than what we used before in [Eq. (6)], where A_k was used to label for the phase modulation amplitude related

to a specific spatial frequency k , instead of that of the entire spectrum $\{k\}$.

From the shown data it is observed, that by making use of an image plane target distribution (circle markers) instead of a single spatial frequency mirror topography (dashed lines), the first order diffraction efficiency is increased. However, we do observe that 20% intensity is still diffracted to higher order spots when the central beam becomes fully attenuated, although this may also be due to a limitation in the current numerical methods that we use. A possible explanation for this effect is given by the fact that at increasing attenuation of the central spot, the phase modulation amplitude that is responsible for the two first order diffraction spots increases. Consequently, this also leads to an increase of the higher order diffraction spot intensities at the image plane. In principle, the amount of phase that must be compensated to cancel the generation of the higher order beams is numerically known, and accounted for by the mirror pattern reconstruction. However, what is currently not accounted for in the reconstruction routine is the special case, in which the phase modulation amplitude correction of these higher orders exceeds the threshold phase of $\sim \pi/6$ rad [also see Eq. (9), and Fig. 3]. In that case, an iterative scheme must be used that also accounts for the resulting higher harmonics. This correction is not yet performed in the current work that is presented here.

Another effect that leads to the generation of the higher orders is the neglect of the amplitude contrast at the mirror plane. When we propagate the targeted image plane distribution towards the mirror plane, the resulting wave front distribution shows both an amplitude and a phase modulation. In the foregoing analysis, we were required to neglect the amplitude information and instead assume a uniform amplitude distribution at the mirror plane, as with a single mirror we can only realize phase modulation.

We can include the effect of amplitude modulation to our calculations, by making use of two mirror reflections. In the image plane reconstruction routines, we then assume that first mirror reflection enables the required amplitude modulation at the second mirror plane. With this modification in place, we can show that the diffraction efficiency is increased. This is indicated by the square markers in [Fig. 9]. From this, it is observed that all intensity of the central beam can be directed into the first order positive and negative diffraction spot.

For use as a beam splitter in Quantum Electron Microscopy, it is necessary that the intensity of the central beam is directed into only either the positive, or negative first order diffraction spot. Optically this would be performed by a blazed grating, which adds a linear phase ramp into the reflected wave front. Blazed grating diffraction has already

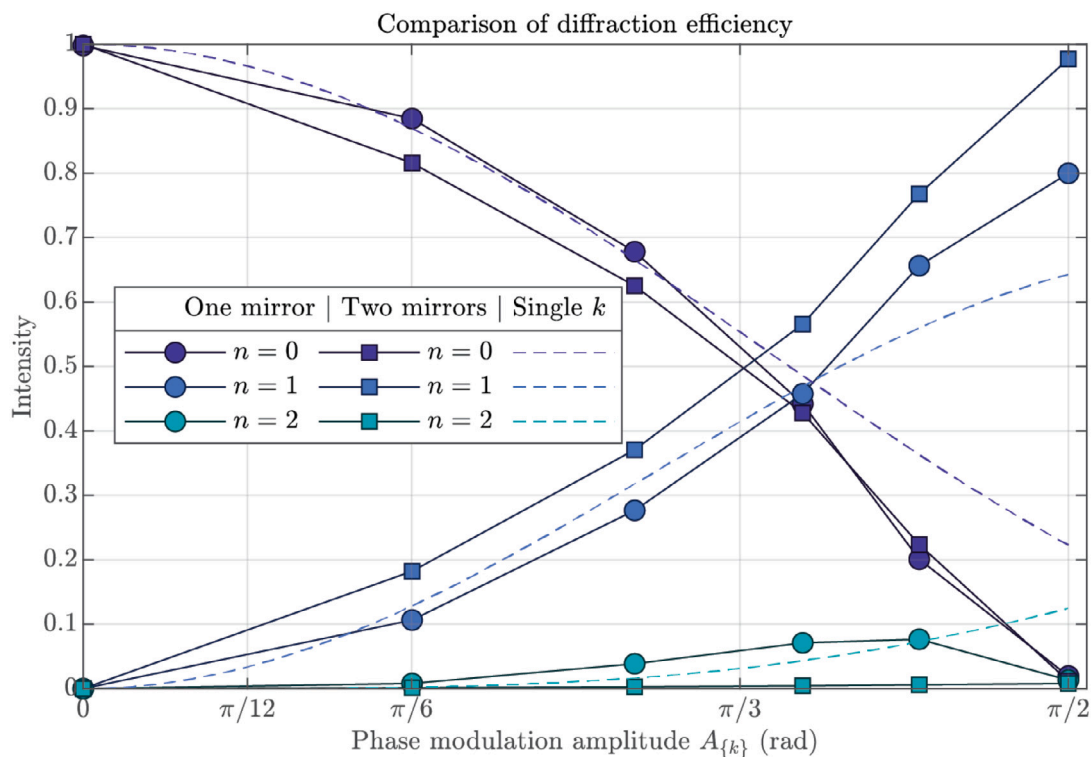


Fig. 9. First order diffraction spot intensity dependence on the mirror patterning approach. The first order diffraction spot intensity at the image plane that results from the use of one spatial frequency in the mirror pattern (dashed line) can be increased by inclusion of higher order spatial frequencies into the pattern. We demonstrate the efficiency that can be reached when performing phase-only modulation with one patterned mirror (circles), and when performing phase and amplitude modulation by using two mirrors (squares). Shown intensities are the sum of positive and negative contribution per order.

been demonstrated in TEM with phase plates [52]. We have studied the feasibility of doing this with one electron mirror by providing a phase-only distribution at the mirror plane, and gradually increased the phase modulation amplitude of this phase ramp. We note that such computation can in principle also be performed by starting out with a target wave front at the image plane and propagate this wave front towards the mirror plane. However, this would require a significant increase of the numerical grid at the image plane without any expected advantages in terms of accuracy of the wave front description at the image plane.

In [Fig. 10] the obtained intensity of the central spot (circles), blazed spot (rectangles), and other spots combined (triangles) is plotted as a function of the maximum phase modulation amplitude $A_{\{k\}}$ across the entire spectrum of the linear phase ramp at the diffraction plane. From this it is seen that a high diffraction efficiency can be obtained especially for weak or strong exchange of spot intensity between the central and blazed spot. The maximum intensity loss towards other orders is limited to 19% and is found when the intensities of the central and blazed spots are equal.

A direct comparison of the potential variation near the turning point of the beam, in the case of (a) regular and (b) blazed diffraction is provided in [Fig. 11]. In the figure, the bold lines indicate the shape of the equipotential at the classical turning point of the beam. Each next equipotential is obtained in steps of 0.5 V, and these are included in the plot to demonstrate how the higher spatial frequency components in the field attenuate faster away from the mirror electrode than the slower spatial components. Also, from the shown equipotential lines the importance of working with a beam with low energy spread can be directly understood, as the spatial components that create the characteristic shape of the equipotential lines attenuate within the range of energy spread of a conventional Schottky source that is not monochromatized.

For the regular diffraction we observe the fundamental spatial frequency that is associated with the first order diffraction, and near the classical turning point an additional higher spatial component is visible as well. It is the higher spatial component that provides attenuation of the undesired higher order beams that result from the fundamental frequency.

The equipotential lines that are associated to the blazed diffraction pattern exhibit a distinct (near)-linear slope. This is to be expected for blazed diffraction, as a linear phase ramp must be added to the reflected beam and the phase scales proportional to the square root of the potential. From the equipotential lines above the classical turning point the fast attenuation of higher spatial frequencies in the field is observed, and at approximately 5 V above the classical turning point only the fundamental frequency is distinctly visible.

4.3. Beam mode conversion

The conversion of plane waves into vortex beams has gained increasing interest in the recent decade. Vortex beams are solutions to the Schrödinger equation in cylindrical coordinates and are characterized by carrying an Orbital Angular Momentum (OAM, ℓ), which expresses itself through an azimuthal component in the wave front [15,16].

Vortex beam generation in TEM can be realized both by using a phase plate, or an amplitude mask. On a phase plate, a spiral ramp is applied [15], where as in the case of an amplitude mask a diffraction grating pattern with a dislocation at the optical axis is used [16]. The number of dislocations N then dictates the Orbital Angular Momentum (ℓ) that is added into the diffracted beam.

With the use of one mirror, we can only adjust the phase of the reflected electron and thus the proper mirror pattern can be obtained by modeling a spiral phase pattern at the mirror plane. Such phase pattern is shown in [Fig. 12(d)] and corresponds to $\ell = 3$ here. In [Fig. 12(a)]

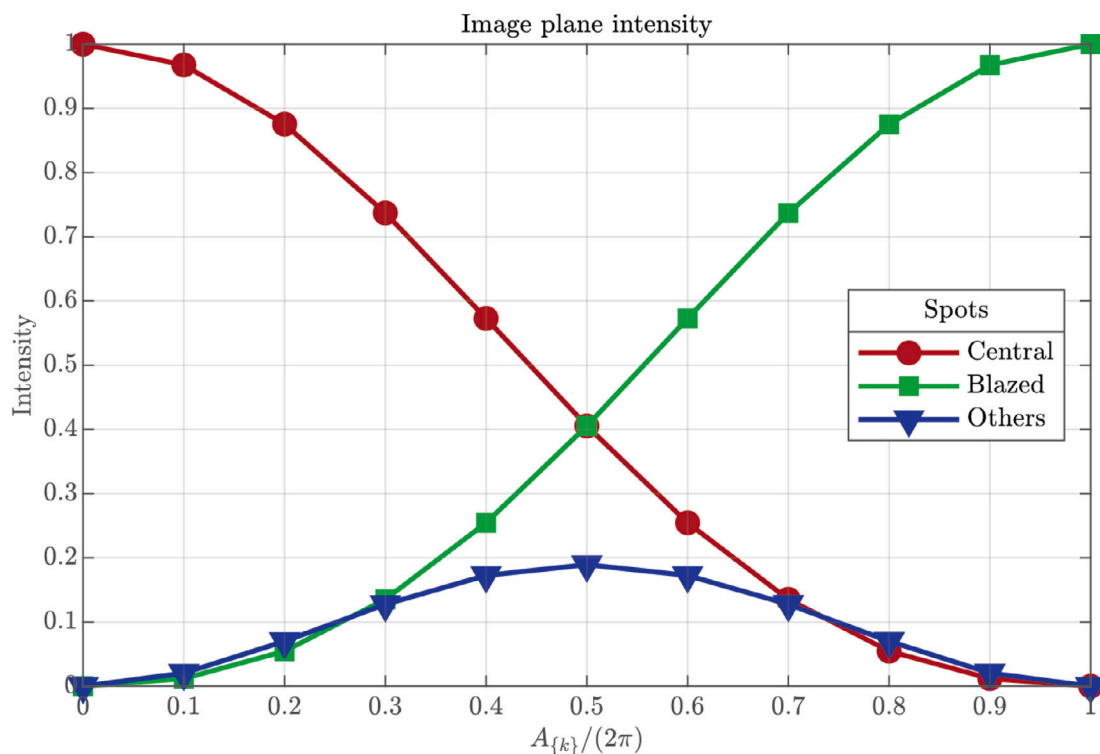


Fig. 10. Blazed grating diffraction efficiency with one electron mirror, as a function of phase modulation amplitude $A_{[k]}$ of the linear phase ramp at the diffraction plane. The values of $A_{[k]}$ are realized by adjusting the ratio of the targeted central and blazed diffraction spot intensities at the image plane. The blazed spot intensity (squares) indicates the intensity of the first order positive diffraction spot.

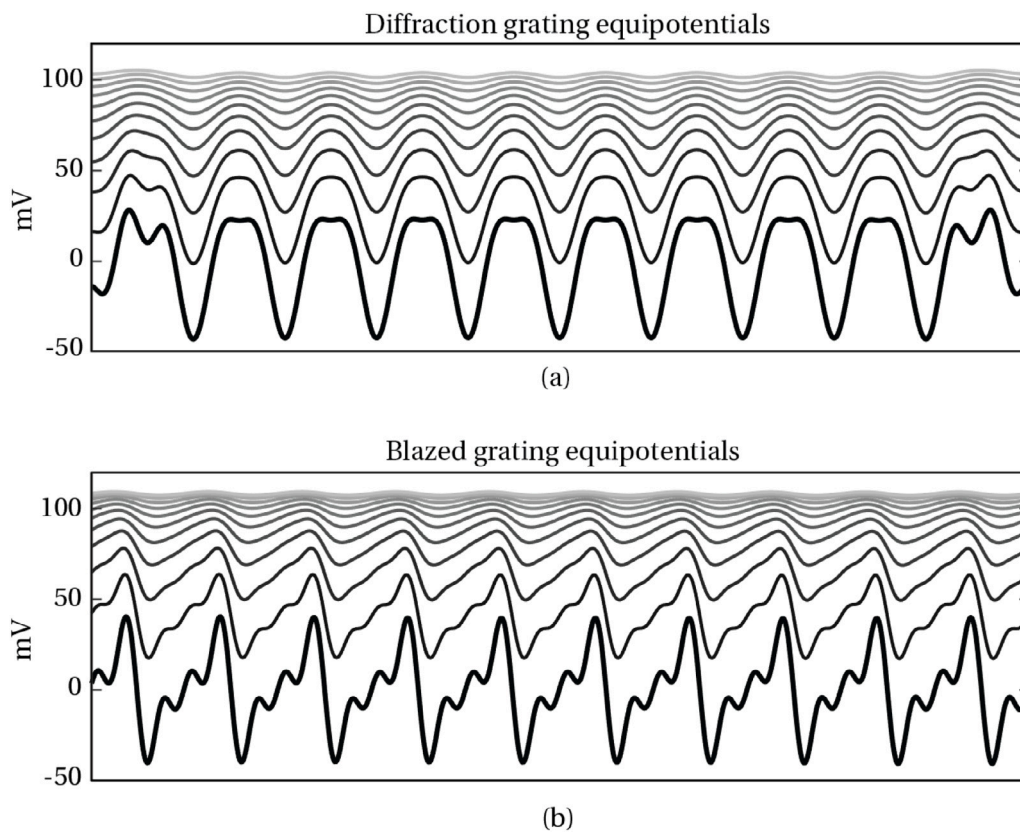


Fig. 11. Comparison of the potential landscapes corresponding to (a) a regular diffraction pattern and (b) a blazed diffraction mirror pattern near the classical turning point z_R . The bold line plots the potential at the classical turning point (-2000 V), and each consecutive line is obtained in steps of 0.5 V.

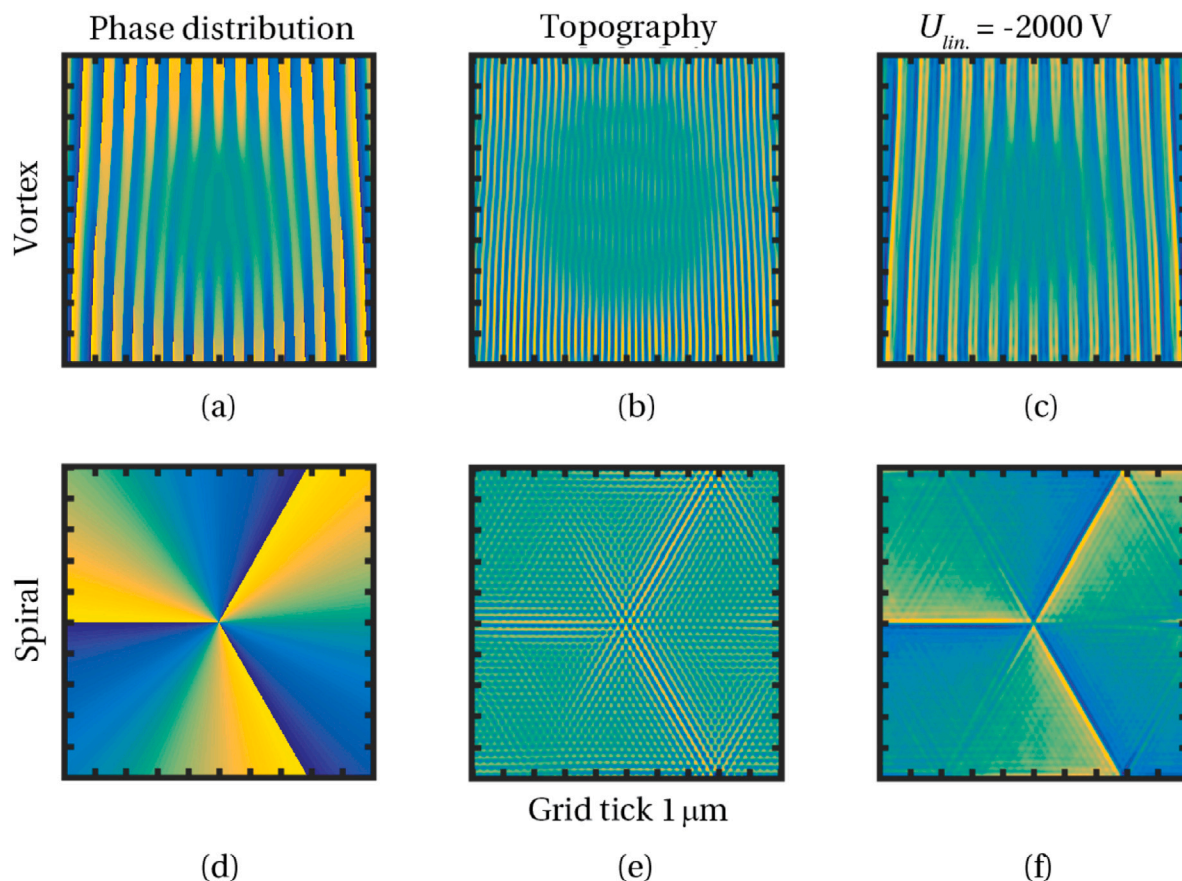


Fig. 12. Two methods for beam mode conversion from plane wave illumination to an orbital angular momentum carrying beam. Reflection on the vortex pattern (a-c) generates a diffraction pattern, in which the diffracted beams carry orbital angular momentum. Two dislocations are applied in this pattern, leading to a lowest value $\ell = \pm 2$ in the reflected beam. The amplitude of the topography modulation in the central region of (b) equals 20 nm. Reflection on the spiral pattern (d-f) generates an on-axis spot with orbital angular momentum, with $\ell = 3$ in the presented case. (Last column) For both patterns, the potential at the classical turning point is shown and these display resemblance to the phase or amplitude masks that would produce a similar effect in TEM. Colormap ranges: phase distribution $[-\pi, \pi]$, topography ± 400 nm (vortex) and ± 200 nm (spiral) and ± 2 mV at the classical turning point. Results obtained for pattern bias potential of 3 V.

we show the equivalent phase pattern that corresponds to a diffracted beam with $\ell = \pm 2$ in the first order.

The reconstructed mirror pattern topographies are shown in [Fig. 12(b, e)] and consist of high spatial frequency components with an amplitude of up to ± 400 nm (b) and ± 200 nm (e) at the edges. Near the center of the vortex pattern, the profile height amplitudes are smaller and range around ± 20 nm. We note that overall, the spatial frequencies in the mirror pattern appear higher than those observed at either the phase pattern at the diffraction plane, or the potential variation near the classical turning point. This is explained by the attenuation of high frequency components, which occur faster away from the mirror electrode compared to the lower frequency components. Hence, the profile amplitude of these higher spatial frequencies at the mirror electrode are relatively high in comparison to the lower spatial frequencies, in line with the observations made in [Section 2.3]. The effect of the high spatial frequency components in the pattern quickly attenuates in the electric field, as can be observed from the potential variation around the averaged coordinate of the turning plane [Fig. 12(c, f)]. At this plane, a potential modulation of ± 2 mV remains, and the shape of the potential variation mimics closely to that of the targeted phase distribution at this plane.

4.4. Arbitrary phase and amplitude modulation

We conclude this section with a demonstration of the generality of electron beam modulation with patterned mirrors. For this, we attempt to create a probe at the image plane after a double mirror reflection

that shows resemblance to the institute logo of Delft University of Technology. The logo contains a flame, and our goal here is to obtain the mirror patterns that are required to realize the amplitude and phase modulation as shown in [Fig. 13(a)]. As a first step, the targeted image plane distribution is Fresnel propagated to the first mirror plane. This provides us with the amplitude and phase distribution that we must imprint into the beam. However, note that a mirror cannot be used for near field amplitude modulation. Hence, we consider here the situation where mirror 2 is positioned in the Fourier plane of mirror 1. We can then realize the required amplitude distribution in front of mirror 2, by means of phase modulation at mirror 1. We then use the reflection at mirror 2 to add the phase modulation, such that at a Fourier plane of mirror 2 the target wave front is realized.

In [Fig. 13(b)] we show the Fourier spectrum of the phase components that must be added by mirror 2. From this data it is seen that a large number of spatial frequencies are required in the mirror pattern. Note, however, that all of the required phase modulation amplitudes satisfy $A_k \leq 0.2$ rad, which in turn is well below the limit for addition of multiple spatial frequencies of $\pi/6$ rad as set forth in [Section 2.1.5]. Based on this spectrum, the mirror topography is constructed and the result of this is shown in [Fig. 13(c)]. The resulting modulation of the electric potential in the vicinity of the classical turning point, corresponding to the plane at which the linear electric potential equals -2 kV, is shown in [Fig. 13(d)].

Admittedly, this result is not very intuitive as it does not clearly resemble any feature of our targeted image plane distribution. In order to verify the effect on the beam at the image plane after the double

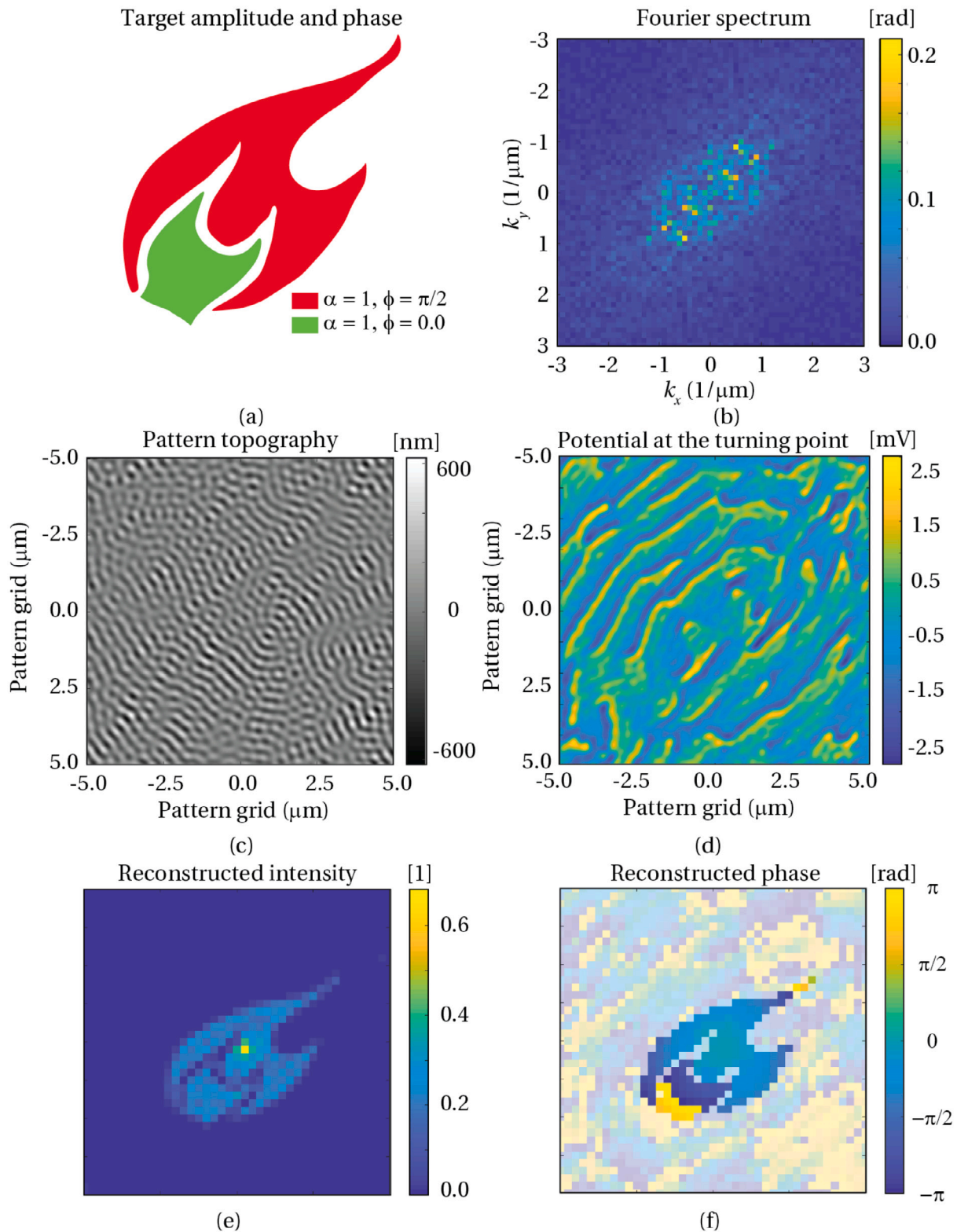


Fig. 13. Demonstration of controlled amplitude and phase modulation with two patterned mirrors. (a) Target amplitude and phase at the image plane. (b) Fourier spectrum of target phase modulation amplitude in front of mirror 2. (c) Pattern topography of mirror 2. (d) Electric potential variation in the vicinity of the classical turning point plane of mirror 2. (e) Reconstructed intensity at the image plane after double mirror reflection. (f) Reconstructed phase distribution at the image plane after double mirror reflection, with partial transparency at pixels for which the reconstructed intensity is less than 0.05 for visual clarity.

mirror reflection, we reconstruct the wave front directly after the reflection at mirror 2 through [Eq. (8)], and by multiplying this result with the amplitude distribution that resulted from the reflection at mirror 1, as we currently do not yet have a proper model for propagating the

reflected beam from mirror 1 onto mirror 2. The obtained intensity and phase distribution at the image plane are shown in [Fig. 13(e-f)] and here we can identify what shows a resemblance with the targeted image plane distribution. The recovery of the targeted image plane

distribution as demonstrated here provides us an initial evidence for the feasibility of controlled wave front shaping with two patterned electron mirrors.

5. Discussion and conclusion

We outlined above that in principle it is possible to gain control over the electron beam wave front through the application of two patterned electron mirrors. This may be referenced to methods in light optics, where the use of two spatial light modulators (SLMs) and polarizers [53], or the use of multiple deformable mirrors [54] enable full spatial beam control.

The effect that a mirror pattern has on the phase of the reflected wave front can in principle be obtained through an existing convolution model, that we discussed in [Section 2.1.1]. Lichte made use of this model when he successfully demonstrated its use for the measurement of the roughness of ‘supersmooth’ electrodes by using electron mirror interference microscopy [25]. The validity of this method is however limited to situations where the mirror roughness is much smaller than the distance of closest approach of the electron beam towards the mirror electrode. This is generally not the case for electron mirrors that are intentionally being patterned, especially for the micromirror setup that we are currently designing [43].

For this reason, we have generalized the method by numerically obtaining the phase difference through application of the WKB method. In fact, our method of integrating the electric field along the crest and trough of the modulated field to obtain the phase modulation shows some form of analogy to the experimental work of Lichte, when one considers the integral along the crest and trough as the object and reference beam in an interference microscope. Regardless, for this we must rely on the validity of the WKB approximation in the vicinity of the turning point of the electron beam. The validity of this has been suggested by our earlier calculations [36] on grating mirrors that are characterized with a single pitch value. We have compared our WKB method to the example data of figure 5 in [25]. For this comparison, we estimated from the cited work a mirror field length of $z_1 = 6$ mm and found a good agreement, indicating that our method converges to the convolution model at large values of pitch. At the same time, we have demonstrated empirically that the validity of the convolution model breaks down whenever $z_R \leq 2h$, i.e., when the beam approaches the mirror pattern to within the height variations inside that pattern.

Further, we have assumed the generality of the method and have motivated that linear addition of the effect of multiple spatial frequencies in the mirror topography is at least valid when the individual components do not add more than $\pi/6$ rad phase modulation to the reflected wave front. If we prefer to include stronger phase modulation terms, this would require some form of iterative scheme that removes the unwanted higher order spots that form during the first step of the topography construction.

The use of replaceable, or otherwise dynamically programmable mirror patterns would significantly increase experimental flexibility. Although we recognize that this is technologically challenging, we also stipulate the advantage that the backplane of the mirror does not obscure the beam path, thus leaving plenty of access for any control logic or circuitry. A good deal of progress with programmable mirrors is made in the past with the development of Reflective Electron Beam Lithography (REBL) [27]. Albeit that the geometry of the mirrors in the REBL deviate from our implementation, since the REBL mirror contains an individual Einzel lens in front of each pixel, it has demonstrated the use of CMOS technology for (individual) addressing of mirror pixels through the back plane of the device. If a practical linear mirror field strength of $E_z = 10$ kV/mm is assumed, this yields a correspondence between pattern profile amplitude and pixel potential of $U = E_z \delta / \delta_0 \approx 10$ mV/nm. The use of pixelwise programmable mirrors instead of relying on a topographic pattern would require a smoothness that is

less strict than that of an etched pattern, under the assumption that each pixel can be addressed individually.

The advantage of a pixelwise programmable mirror instead of a topographic patterned mirror is also apparent from the ability to correct for mechanical tolerances. Tilt is the simplest form of a mechanical error that can arise in a mirror setup. The effect of tilt is a linear field strength gradient perpendicular to the optical axis. This resembles a dipole field that acts perpendicular to the electron beam propagation and results in a sideways beam deflection.

The effect of this dipole field on the beam deflection can be approximated. For an assumed mirror tilt angle θ , and beam width w , the dipole strength along the propagation axis becomes $E_2 = U\theta w / (z_1(z_1 + \theta w))$. Here, z_1 is the length of the mirror field, and U the mirror electrode bias potential. In most practical cases, $\theta w \ll z_1$. For an average beam energy in the mirror field equal to half the electrode potential, the deflection angle in the field may then become approximately given as $\alpha \approx 2\theta w / z_1$, if we assume a top hat field distribution. In a setup that we are currently developing, we have $w = 10$ μm , and $z_1 = 200$ μm , which leads to $\alpha \approx 0.1\theta$, i.e., the deflection due to a tilt error equals roughly 10% of that tilt error. With the use of silicon based mirror electrodes and flat glass spacers, the tilt error is easily limited below $\theta \leq 1$ mrad.

Other optical effects may arise from the non-flatness of the mirror electrode that extends the mirror pattern topography. Non-flatness can arise for instance from mechanical stress in the mirror electrode. Stress in one direction may lead to astigmatism in the reflected beam, and the effect of this on the reflected beam can actually be modeled by adding a spatial frequency with the assumed curvature into the mirror calculations. In reference to [Fig. 5] we note that a beam width of 10 μm (i.e., a spatial frequency of 0.1 μm^{-1}) already adds phase modulation amplitude to the reflected beam when the curvature of the electrode is in the order of single or double digit nanometers, depending on the bias potential. While we recognize the non-flatness of the mirror electrode as a possible technology barrier during the initial development of a double mirror system based on topographic patterned mirrors, the development of pixelwise programmable mirrors will offer a solution to this limitation.

We conclude the discussion on optical effects by noting that the high coefficient of spherical aberration that is usually associated with flat electron mirrors can to a large extent be compensated for by the geometry of the imaging lens in between the mirror electrode and the image plane [55]. For use of the virtual phase plate with high energy electron beams, such as those found inside a transmission electron microscope, we recognize the risk of electrical breakdown as one of the main limitations. As we rely on mirrors, this implies slowing down of the incident beam to zero kinetic energy and thus the mirror potential must always be slightly more negative than that of the electron source cathode. However, we believe that this issue can be circumvented for instance by placing the double mirror system in front of the beam accelerator, close to the source module of the microscope.

Controlled wave front shaping requires a coherent electron beam. As the degree of coherence is directly related to the reduced brightness B_r of the source, a high-quality source is required. For a coherent beam, the beam current must be limited to less than $I_{\text{beam}} \leq 10^{-18} B_r$ [8]. In practice this leads to a beam current in the order of 1 – 100 pA for a Schottky source. The throughput of the microscope then becomes limited as a trade off for beam coherence, as is similar to other phase plate techniques.

Finally, we discuss various opportunities that present themselves even when only fixed mirror patterns are used. In the integrated double mirror setup as it is shown in [Fig. 7], there is room for the placement of a specimen in between the two mirrors at the mirror axis, at the cross-over plane of the beam next to the electrostatic deflector. If one would apply a grating pattern on both the top and bottom mirror, the diffractive action of both mirrors constitutes an amplitude splitter (first mirror) and amplitude combiner (second mirror). Placement of

a specimen in the common cross over plane of the mirror axis that may or may not block the surroundings of the mirror axis, while leaving the on-axis region free, creates a Mach–Zehnder interferometer and thus enables an experimental demonstration of interaction-free measurement for electrons [45,46].

As a next step, we now imagine further possibilities when pulsed operation of the electrostatic deflector on the optical axis becomes possible. When given the possibility to double the low-voltage deflection field strength of this deflector within the time spent by the electron at the mirror axis, the electron will be cycled back to the mirror axis upon passing the deflector for the second time, since the deflection angle doubles as well. This would enable multi-pass interaction free measurements with electrons [56]. When a grating pattern is used as beam splitter and combiner, the setup also offers a feasible method for experimentally performing quantum electron microscopy [49], although additional alignment difficulties must be considered for this [50]. Of course, this would only demonstrate the principles of quantum electron microscopy, because a real application on beam sensitive materials would require at least 60 keV beam energy instead of the 2 keV that was used in our calculations.

In conclusion, we have described a novel microscopy scheme that could potentially enable the manipulation of both phase and amplitude of an electron beam. This is realized by using two patterned electron mirrors inside a microscope. The scheme makes use of reflective electron optical components to modulate the phase of the reflected wave front, and in this way we expect to avoid typical issues that are encountered in transmission based approaches to beam shaping.

Data availability statement

The data that support the findings of this study are available from the corresponding author upon reasonable request.

Acknowledgments

The authors would like to acknowledge discussions within the Quantum Electron Microscopy collaboration. This work is funded in part by the Dutch Research Council (NWO), and in part by the Gordon and Betty Moore Foundation (GBMF) as part of the QEM collaboration.

Declaration of competing interest

Declaration of interest and prior art. Author P. K. holds a patent (WO2018016961A1, Aberration correcting device for an electron microscope and an electron microscope comprising such a device) that relates to the techniques described in this work. Author M. K. has previously published (parts of) this work as a PhD thesis chapter [57].

Appendix A. Turning point coordinates through the Lambert-W function

The classical turning point z_R^\pm for the most and least nearest approach of the beam towards the mirror with a modulated potential are found by equating the scalar electric field to the cathode potential E at the source,

$$U(x_\pm, y_\pm, z_R^\pm) = u_0 \left[1 - \frac{z_R^\pm}{z_1} \right] \pm F_{n,m} \exp(-2\pi k_0 |z_R^\pm|). \quad (35)$$

Solutions to these equations are provided by the Lambert-W function, in the form of [42],

$$z_R^\pm = \frac{1}{2\pi k_0} \times \frac{-AW_0 \left(-A^{-1} \exp \left[-\frac{B}{A} \right] \right) - B}{A}. \quad (36)$$

In this equation,

$$A = \pm \frac{u_0}{2\pi F_{n,m} k_0 z_1}, \quad B = \pm \frac{E - u_0}{F_{n,m}}, \quad k_0 \equiv k_z = 2\pi \sqrt{k_{n,x}^2 + k_{m,y}^2}.$$

(37)

In MATLAB, use of the function `lambertw(k, x)` enables the calculation of k th branch of the Lambert function, evaluated at x [58]. Solutions for z_R^\pm are obtained from the zero-th (principal) branch.

Appendix B. Numerical methods

We use MATLAB for all numerical calculations. The numerical work consists of the following subroutines:

- WKB approximation solver.
- WKB lookup table interpreter.
- Fresnel propagator.
- Target phase and amplitude solver.
- Scalar potential constructor.

In the following sections we discuss the specifics for implementing the above listed routines into MATLAB.

B.1. WKB approximation solver

The WKB approximation [Eq. (5)] is numerically evaluated for a single parameter set consisting of spatial frequency (k_0), pattern amplitude (δ_0), cap electrode spacing (z_1) and excitation parameters beam energy (E), and pattern potential (U_{pattern}). The WKB approximation is calculated along two trajectories that run parallel to the propagation (z) axis and coincide with a crest and through of the considered spatial frequency, in accordance with [Eq. (6)].

The WKB approximation integral is computed over the full length of the two axes, and is terminated at points z_0 and z_1 . To this end, we first calculate the integrated momentum along the both trajectories. This procedure generates complex valued results, as the argument to the square root becomes negative as $|z| < |z_R|$. We only keep the real valued part, as this represents the data in front of the turning point.

Listing 1: Definition of axial momentum for crest and trough field.

```

1 % Zero pitch potential
2 U_zero = @(z) Up*(1+1/d*(+delta*exp(2*pi*kp*z)-z));
3 % Half pitch potential
4 U_half = @(z) Up*(1+1/d*(-delta*exp(2*pi*kp*z)-z));
5
6 % Electron momentum per axis
7 p_zero = @(z) real( sqrt(2*mee*(E-U_zero(z))) );
8 p_half = @(z) real( sqrt(2*mee*(E-U_half(z))) );

```

As the non-linear behavior of the electric potential is confined in the region close to the turning point $z_R \approx z_0$, the numerical integration is performed on logarithmically spaced waypoints, with increased waypoint density near z_R .

Listing 2: Definition of axial momentum for crest and trough field.

```

1 % Definition of waypoints for integration.
2 waypoints = -logspace( log10(-z1), -9,
   number_of_waypoints);
3 % Numerical integration and phase extraction.
4 int_zero = 2/hbar*integral(p_zero, z1, z0, 'WayPoints
   ', points);
5 int_half = 2/hbar*integral(p_half, z1, z0, 'WayPoints
   ', points);
6 % Phase in correspondence with [Eq. (3.5)]
7 phi = int_zero - int_half;

```

B.2. WKB lookup table generator

The WKB lookup table data, as shown for three reference amplitudes in [Fig. 5] is generated by repetitive calls to the WKB approximation routine. The lookup tables that are used for this work are obtained for parameter space $\mathcal{E} = 2$ keV, linear field strength $E_z = 10$ kV/mm ($z_1 = -200$ μm) and 10^5 waypoints in the WKB approximation integral. The construction of the lookup table data is a relatively time consuming task, but has to be performed in principle only one time. We note that the use of a lookup table reduces the calculation time at a later stage, when the data is used to construct mirror topographies.

Listing 3: WKB lookup table generator.

```

1 for k0 = list_k0
2   for Up = list_Upattern
3     WKB_data(i_k, i_U) = WKB_approximation( k0,
4       delta0, 'PatternPotential', Up, '
5         BeamEnergy', E0, 'ApertureSpacing', z1,
6         'NumberOfWaypoints', 1e5);
7   end
8 end

```

The generated data matrix `WKB_data` and the associated list of spatial frequencies and bias potentials are stored and used as lookup table during the pattern reconstruction. We make use of linear interpolation in the spatial frequency data points in order to compute a pattern frequency component that is not part of the original lookup data.

Listing 4: Obtaining the profile scaling parameter for a target phase.

```

1 % Find interpolated reference amplitudes (for 1 AA).
2 phase_per_reference_amplitude = interp1(k0, WKB_data,
3   pattern_k0_values);
4 % Scale with respect to the required angle.
5 amplitudes = delta0 ./ phase_per_reference_amplitude
6   .* (myPhaseTerms);

```

B.3. Fresnel propagator

The relationship between image plane (ψ_1) and diffraction plane (ψ_M) distributions is described by a Fresnel propagation and intermediate lens action [41],

$$\psi_M = \underbrace{\left(\psi_1 * \exp \left[-i2\pi k_e \frac{R^2}{2f} \right] \right)}_{\text{Propagation}} \times \underbrace{\exp \left[i2\pi k_e \frac{R^2}{2f} \right]}_{\text{Focusing}}. \quad (38)$$

In the equation, the wave front ψ_1 at the common cross-over plane is convoluted (*) with a propagation function that depends on the modulus of the beam wave number (k_e), transverse radial coordinate perpendicular to the optical axis (R) and focal length (f) of the lens, and next focused by the focusing term.

Listing 5: Fresnel propagation from image to diffraction plane.

```

1 % Based on Cowley (1975) Ch. 3, Fresnel propagator.
2 prop = exp( -1i*2*pi*k*(X.^2+Y.^2)/(2*f));
3 lens = exp( 1i*2*pi*k*(X.^2+Y.^2)/(2*f));
4 % Obtain the complex wave function at the diffraction
5   plane
6 % This calculation may take a while, depending on the
7   image size.
8 diffraction_plane = conv2(psi1, prop, 'same') .* lens
9   / sqrt(numel(lens));

```

B.4. Target phase and pattern solver

The Fourier transform of the phase distribution at the mirror plane is obtained and the complex valued terms provide the basis for the pattern reconstruction. For each phase value of the Fourier term and associated spatial frequency, the WKB lookup is performed on the magnitude of the Fourier term. This provides the amplitude for this mirror topography contribution. The complex angle of the Fourier term is used in the reconstruction of the mirror pattern in order to provide proper relative positioning of the wave components. The number of Fourier terms that is considered is limited by a threshold value that can be set arbitrarily close to zero. The threshold allows to limit computation time by skipping very high frequency components that add virtually no phase to the reflected beam, or that would otherwise result in an excessive pattern profile height.

Listing 6: Relating phase to pattern topography.

```

1 reduced_diffraction_plane = angle(diffraction_plane);
2
3 % Obtain spectral components of the angle
4   distribution.
5 spectral_components = fft2(reduced_diffraction_plane)
6   / numel(reduced_diffraction_plane);
7 spectrum = fftshift(spectral_components);
8
9 % Loop over all spectral components
10 for row = 1:length(ky)
11   for col = 1:length(kx)
12     thisPhi = abs(spectrum(row, col));
13     thisK = sqrt( kx^2 + ky^2 );
14     % WKB lookup
15     amplitude = WKB_lookup(WKBdata, thisPhi,
16       thisK, Up);
17     % Add the geometrical pattern angle to this
18     value
19     GeoAngle = angle(spectrum(row, col));
20     % Save for pattern reconstruction
21     reconstruct(end+1,:) = [ky kx amplitude*exp(1
22       i*GeoAngle)];
23   end
24 end

```

The mirror topography is reconstructed based on the coefficients that were obtained in the previous step. For each spatial component, the contribution to the topography is determined as a Fourier term.

Listing 7: Reconstructing the mirror topography.

```

1 % reconstruct = (3x1) double complex [ky kx amp*exp
2   (1i*phi)]
3 full_field = zeros(size(X));
4 for index = 1:size(reconstruct,1)
5   el = reconstruct(index,:);
6   ky = real(el(1));
7   kx = real(el(2));
8   % Verified reconstruction sum.
9   component = abs(el(3)) .* ( cos( 2*pi*(kx.*X + ky
10     .*Y) + angle(el(3)) ) );
11   full_field = full_field + component;
12 end
13 % Scale the field to units of nanometer.
14 full_field = 1e9 * fftshift(full_field);

```

B.5. Scalar potential constructor

The shape of the scalar electric potential, as a function of pattern topography is calculated in accordance with [Eq. (23)]. We make use of anonymous function declarations in MATLAB for this calculation.

Listing 8: Scalar potential reconstruction.

```

1 % Bias at analysis point (zz), assuming U1 = 0.
2 U0 = Up*(1-(zz/z1));
3 % Modulated potential as Anonymous function.
4 UU = @(X,Y,zz, kx, ky, amp, theta)
5
6     amp .* cos( 2*pi*(kx.*X + ky.*Y) + theta ) *
7     exp(-abs(zz)*2*pi*sqrt(kx^2+ky^2) );
8
9 for index = 1:size(reconstruct,1)
10     % Row elements of reconstruction array.
11     el = reconstruct(index,:);
12     kx = real(el(1));
13     ky = real(el(2));
14     amp = abs(el(3));
15     theta = angle(el(3));
16     % Calculate contribution for this term.
17     component = UU(X, Y, zz, kx, ky, amp, theta);
18     potential = potential + component;
19 end

```

References

- [1] C. Maurer, et al., What spatial light modulators can do for optical microscopy, *Laser Photon. Rev.* 5 (1) (2010) 81–101, <http://dx.doi.org/10.1002/lpor.200900047>.
- [2] D. Dudley, W.M. Duncan, J. Slaughter, Emerging digital micromirror device (DMD) applications, in: H. Urey (Ed.), *MOEMS Display and Imaging Systems*, SPIE, 2003, <http://dx.doi.org/10.1117/12.480761>.
- [3] J.B. Sampsel, Digital micromirror device and its application to projection displays, *J. Vac. Sci. Technol. B* 12 (6) (1994) 3242, <http://dx.doi.org/10.1116/1.587506>.
- [4] G. Guzzinati, et al., Prospects for versatile phase manipulation in the TEM: Beyond aberration correction, *Ultramicroscopy* 151 (2015) 85–93, <http://dx.doi.org/10.1016/j.ultramic.2014.10.007>.
- [5] H. Okamoto, T. Latychevskaia, H.-W. Fink, A quantum mechanical scheme to reduce radiation damage in electron microscopy, *Appl. Phys. Lett.* 88 (16) (2006) 164103, <http://dx.doi.org/10.1063/1.2191096>.
- [6] H. Okamoto, Noise suppression by active optics in low-dose electron microscopy, *Appl. Phys. Lett.* 92 (6) (2008) 063901, <http://dx.doi.org/10.1063/1.2870097>.
- [7] J. Verbeeck, et al., Demonstration of a 2×2 programmable phase plate for electrons, *Ultramicroscopy* 190 (2018) 58–65, <http://dx.doi.org/10.1016/j.ultramic.2018.03.017>.
- [8] P. Kruit, Electron sources, in: C.B. Carter, D.B. Williams (Eds.), *Transmission Electron Microscopy*, Springer International Publishing, 2016, pp. 1–15, http://dx.doi.org/10.1007/978-3-319-26651-0_1.
- [9] P.W. Hawkes, Aberration correction past and present, *Phil. Trans. R. Soc. A* 367 (1903) (2009) 3637–3664, <http://dx.doi.org/10.1098/rsta.2009.0004>.
- [10] L. Clark, et al., Exploiting lens aberrations to create electron-vortex beams, *Phys. Rev. Lett.* 111 (6) (2013) <http://dx.doi.org/10.1103/physrevlett.111.064801>.
- [11] D. Willasch, High resolution electron microscopy with profiled phase plates, *Optik* 44 (1) (1975).
- [12] R. Danev, K. Nagayama, Phase plates for transmission electron microscopy, in: *Methods in Enzymology*, Elsevier, 2010, pp. 343–369, [http://dx.doi.org/10.1016/s0076-6879\(10\)81014-6](http://dx.doi.org/10.1016/s0076-6879(10)81014-6).
- [13] F. Zernike, Phase contrast, a new method for the microscopic observation of transparent objects, *Physica* 9 (7) (1942) 686–698, [http://dx.doi.org/10.1016/s0031-8914\(42\)80035-x](http://dx.doi.org/10.1016/s0031-8914(42)80035-x).
- [14] R. Danev, K. Nagayama, Transmission electron microscopy with zernike phase plate, *Ultramicroscopy* 88 (4) (2001) 243–252, [http://dx.doi.org/10.1016/s0304-3991\(01\)00088-2](http://dx.doi.org/10.1016/s0304-3991(01)00088-2).
- [15] M. Uchida, A. Tonomura, Generation of electron beams carrying orbital angular momentum, *Nature* 464 (7289) (2010) 737–739, <http://dx.doi.org/10.1038/nature08904>.
- [16] J. Verbeeck, H. Tian, P. Schattschneider, Production and application of electron vortex beams, *Nature* 467 (7313) (2010) 301–304, <http://dx.doi.org/10.1038/nature09366>.
- [17] B.J. McMoran, et al., Electron vortex beams with high quanta of orbital angular momentum, *Science* 331 (6014) (2011) 192–195, <http://dx.doi.org/10.1126/science.1198804>.
- [18] S.M. Lloyd, et al., Electron vortices: Beams with orbital angular momentum, *Rev. Modern Phys.* 89 (3) (2017) <http://dx.doi.org/10.1103/revmodphys.89.035004>.
- [19] V. Grillo, et al., Generation of nondiffracting electron Bessel beams, *Phys. Rev. X* 4 (1) (2014) <http://dx.doi.org/10.1103/physrevx.4.011013>.
- [20] N. Voloch-Bloch, et al., Generation of electron Airy beams, *Nature* 494 (7437) (2013) 331–335, <http://dx.doi.org/10.1038/nature11840>.
- [21] R.M. Glaeser, Invited Review Article: Methods for imaging weak-phase objects in electron microscopy, *Rev. Sci. Instrum.* 84 (11) (2013) 111101, <http://dx.doi.org/10.1063/1.4830355>.
- [22] D. Preikszas, H. Rose, Correction properties of electron mirrors, *J. Electron Microsc. 46* (1) (1997) 1–9, <http://dx.doi.org/10.1093/oxfordjournals.jmicro.a023484>.
- [23] G.F. Rempfer, et al., Simultaneous correction of spherical and chromatic aberrations with an electron mirror: An electron optical achromat, *Microsc. Microanal.* 3 (1) (1997) 14–27, <http://dx.doi.org/10.1017/s143192769797001x>.
- [24] A. Bok, et al., Mirror electron microscopy, in: *Advances in Imaging and Electron Physics*, Elsevier, 2017, pp. 99–192, <http://dx.doi.org/10.1016/bs.aiep.2017.07.005>.
- [25] H. Lichte, G. Mollenstedt, Measurement of the roughness of supersmooth surfaces using an electron mirror interference microscope, *J. Physics E* 12 (10) (1979) 941–944, <http://dx.doi.org/10.1088/0022-3735/12/10/014>.
- [26] H. Okamoto, Adaptive quantum measurement for low-dose electron microscopy, *Phys. Rev. A* 81 (4) (2010) <http://dx.doi.org/10.1103/physreva.81.043807>.
- [27] A.M. Carroll, Pattern generators for reflective electron-beam lithography (REBL), in: *Advances in Imaging and Electron Physics*, Elsevier, 2015, pp. 1–23, <http://dx.doi.org/10.1016/bs.aiep.2015.02.001>.
- [28] H. Muller, D. Preikszas, H. Rose, A beam separator with small aberrations, *J. Electron Microsc. 48* (3) (1999) 191–204, <http://dx.doi.org/10.1093/oxfordjournals.jmicro.a023670>.
- [29] R.M. Tromp, et al., A new aberration-corrected, energy-filtered LEEM/PEEM instrument. I. Principles and design, *Ultramicroscopy* 110 (7) (2010) 852–861, <http://dx.doi.org/10.1016/j.ultramic.2010.03.005>.
- [30] R.M. Tromp, et al., A new aberration-corrected, energy-filtered LEEM/PEEM instrument II. Operation and results, *Ultramicroscopy* 127 (2013) 25–39, <http://dx.doi.org/10.1016/j.ultramic.2012.07.016>.
- [31] M.A.R. Krielaart, et al., Miniature electron beam separator based on three stacked dipoles, *J. Appl. Phys.* 127 (23) (2020) 234904, <http://dx.doi.org/10.1063/5.0008089>.
- [32] H. Dohi, P. Kruit, Design for an aberration corrected scanning electron microscope using miniature electron mirrors, *Ultramicroscopy* 189 (2018) 1–23, <http://dx.doi.org/10.1016/j.ultramic.2018.03.009>.
- [33] H. Rose, W. Wan, Aberration correction in electron microscopy, in: *Proceedings of the 2005 Particle Accelerator Conference*, IEEE, <http://dx.doi.org/10.1109/pac.2005.1590354>.
- [34] S.M. Kennedy, et al., Phase sensitivity of slow electrons to interactions with weak potentials, *Phys. Rev. A* 74 (4) (2006) <http://dx.doi.org/10.1103/physreva.74.044701>.
- [35] A.J. Hermans, J.A. Petterson, A quantum mechanical treatment of the mirror electron microscope, *J. Eng. Math.* 4 (2) (1970) 141–154, <http://dx.doi.org/10.1007/bf01535086>.
- [36] M.A.R. Krielaart, P. Kruit, Grating mirror for diffraction of electrons, *Phys. Rev. A* 98 (6) (2018) <http://dx.doi.org/10.1103/physreva.98.063806>.
- [37] M. Vulović, et al., When to use the projection assumption and the weak-phase object approximation in phase contrast cryo-EM, *Ultramicroscopy* 136 (2014) 61–66, <http://dx.doi.org/10.1016/j.ultramic.2013.08.002>.
- [38] R.S. Gvosdover, B.Y. Zel'dovich, The quantum theory of image contrast formation of electric and magnetic microfields in mirror electron microscopy, *J. Microsc.* 17 (107) (1973).
- [39] P.W. Hawkes, E. Kasper, *Principles of Electron Optics*, vol. 3, Academic Press, 1996.
- [40] Handbook of continued fractions for special functions, Springer Netherlands, 2008, <http://dx.doi.org/10.1007/978-1-4020-6949-9>.
- [41] J.M. Cowley, *Diffraction Physics*, Elsevier, 1995.
- [42] R.M. Corless, et al., On the LambertW function, *Adv. Comput. Math.* 5 (1) (1996) 329–359, <http://dx.doi.org/10.1007/bf02124750>.
- [43] M.A.R. Krielaart, *Electron Wave Front Modulation with Patterned Mirrors* (Ph.D. thesis), Delft University of Technology, ISBN: 978-94-6384-202-0, 2021, Ch. 4, URL <https://doi.org/10.4233/uuid:285e9079-e12c-4cd4-9a3a-555bf66237c7>.
- [44] J.M. Zuo, J.C.H. Spence, *Advanced Transmission Electron Microscopy*, Springer New York, 2017, <http://dx.doi.org/10.1007/978-1-4939-6607-3>.
- [45] A.C. Elitzur, L. Vaidman, Quantum mechanical interaction-free measurements, *Found. Phys.* 23 (7) (1993) 987–997, <http://dx.doi.org/10.1007/bf00736012>.
- [46] W.P. Putnam, M.F. Yanik, Noninvasive electron microscopy with interaction-free quantum measurements, *Phys. Rev. A* 80 (4) (2009) <http://dx.doi.org/10.1103/physreva.80.040902>.
- [47] R.F. Egerton, P. Li, M. Malac, Radiation damage in the TEM and SEM, *Micron* 35 (6) (2004) 399–409, <http://dx.doi.org/10.1016/j.micron.2004.02.003>.
- [48] S. Thomas, et al., Semitransparency in interaction-free measurements, *Phys. Rev. A* 90 (5) (2014) <http://dx.doi.org/10.1103/physreva.90.053840>.
- [49] P. Kruit, et al., Designs for a quantum electron microscope, *Ultramicroscopy* 164 (2016) 31–45, <http://dx.doi.org/10.1016/j.ultramic.2016.03.004>.
- [50] M. Turchetti, et al., Design and simulation of a linear electron cavity for quantum electron microscopy, *Ultramicroscopy* 199 (2019) 50–61, <http://dx.doi.org/10.1016/j.ultramic.2019.01.010>.

- [51] Y. Yang, et al., Efficient two-port electron beam splitter via a quantum interaction-free measurement, *Phys. Rev. A* 98 (4) (2018) <http://dx.doi.org/10.1103/physreva.98.043621>.
- [52] C.W. Johnson, D.H. Bauer, B.J. McMorran, Improved control of electron computer-generated holographic grating groove profiles using ion beam gas-assisted etching, *Appl. Opt.* 59 (6) (2020) 1594, <http://dx.doi.org/10.1364/ao.376876>.
- [53] L. Zhu, J. Wang, Arbitrary manipulation of spatial amplitude and phase using phase-only spatial light modulators, *Sci. Rep.* 4 (1) (2014) <http://dx.doi.org/10.1038/srep07441>.
- [54] C. Wu, et al., Phase and amplitude beam shaping with two deformable mirrors implementing input plane and Fourier plane phase modifications, *Appl. Opt.* 57 (9) (2018) 2337, <http://dx.doi.org/10.1364/ao.57.002337>.
- [55] M.A.R. Krielaart, P. Kruit, Flat electron mirror, *Ultramicroscopy* 220 (2021) 113157, <http://dx.doi.org/10.1016/j.ultramic.2020.113157>.
- [56] P. Kwiat, et al., Interaction-free measurement, *Phys. Rev. Lett.* 74 (24) (1995) 4763–4766, <http://dx.doi.org/10.1103/physrevlett.74.4763>.
- [57] M.A.R. Krielaart, *Electron Wave Front Modulation with Patterned Mirrors* (Ph.D. thesis), Delft University of Technology, ISBN: 978-94-6384-202-0, 2021, Ch. 3, URL <http://dx.doi.org/10.4233/uuid:285e9079-e12c-4cd4-9a34-555bf66237c7>.
- [58] MathWorks, Lambert W function, 2006, <https://nl.mathworks.com/help/symbolic/lambertw.html>, (Accessed April 2020).